Design and piloted simulator evaluation of adaptive safe flight envelope protection algorithm

Lombaerts, T; Looye, G; Ellerbroek, J; Rodriguez y Martin, MJM

Design and Piloted Simulator Evaluation of Adaptive

Safe Flight Envelope Protection Algorithm

Thomas Lombaerts* and Gertjan Looye†

German Aerospace Center DLR, 82234 Weßling, Germany

Joost Ellerbroek‡ and Mitchell Rodriguez y Martin§

Delft University of Technology, 2629 HS Delft, The Netherlands

This paper discusses the design and evaluation of an efficient safe flight envelope protection method, for keeping an augmented aircraft with manual flight control laws within the safe envelope bounds. This flight envelope is estimated adaptively, so that configuration changes and possible failures can be taken into account. The updated information of the safe envelope is used in the flight control laws to prevent loss of control in flight. It has been found that a control architecture involving separate pilot command filtering is particularly well suited to incorporate these adaptive protections. Moreover, haptic feedback to the pilot controls can be included as well, based on the same adaptive bounds. This has the potential to further increase the flight crew awareness about the risk of losing control in flight. These algorithms have been evaluated in the Simona Research Simulator at Delft University of Technology, to investigate the impact on the awareness of the crew. Commercial airline crews flew multiple challenging approach and landing scenarios in a relevant simulated environment. Results show that the algorithms support the flight crew significantly. They contribute to 'care-free' flying and to avoiding loss of control in flight.

I.   Introduction

WORLDWIDE civil aviation operations are expected to increase significantly in the next decades. This rapid growth will have important consequences. Given the importance of safety in civil aviation, many efforts made in the past have already resulted in a lower number of accidents. However, maintaining the current accident rate would result in an increasing number of accidents, proportional to the growth of traffic. This is not acceptable to the general public. Therefore, in civil aviation, further developments are required which focus on the continuous improvement of safety levels and reducing the risks of life threatening failures. In recent studies by the International Civil Aviation Organization (ICAO) and the Commercial Aviation Safety Team (CAST), it can be observed that loss of control in flight (LOC-I) is the most frequent primary accident cause [1]. LOC-I accidents have a variety of contributing factors, occurring individually or in combination, such as a system malfunction, atmospheric disturbances (e.g., turbulence or icing), and loss of situational awareness by the crew. During operations under system malfunction or atmospheric disturbance the aircraft performance and handling characteristics can degrade abruptly and over time. This needs to be taken into account in the flight control laws, and the flight crew has to be made aware of these changes.

---

*Previously Marie Curie Fellow at DLR, Institute of System Dynamics and Control, Department of Aircraft Systems Dynamics, now aerospace research engineer at NASA Ames Research Center, Intelligent Systems Division, e-mail: thomas.lombaerts@nasa.gov, AIAA Senior Member.

†Department Head at DLR, Institute of System Dynamics and Control, Department of Aircraft Dynamics.

‡Assistant Professor at Delft University of Technology, Faculty of Aerospace Engineering, Control and Simulation Section.

§Previously Aerospace Engineering Student at Delft University of Technology, Control and Simulation Section, now Simulator Maintenance Engineer at Aerosertec, Airbus Defence & Space.

American Institute of Aeronautics and Astronautics

The CAST established a specialized international safety analysis team to study the apparent growing trend in loss of Airplane State Awareness (ASA) by the flight crew. This team published recommended safety enhancements that include the research, development, and implementation of technologies for enhancing flight crew awareness of airplane energy state (SE 207) [2] as well as the development and implementation of bank angle protection technologies (SE202) [3]. Previous research addressed these recommendations by interfacing an on-board safe flight envelope estimation capability with cockpit displays [4, 5]. The research presented in this paper builds further on the previous results by implementing this updated safe flight envelope information in a flight envelope protection algorithm as part of the flight control laws to prevent loss of control in flight. Moreover, haptic feedback to the pilot controls can be part of this set-up too, based on the same adaptive bounds. This has the potential to further increase the flight crew awareness about the risk of losing control in flight.

A.   Current state-of-the-art flight envelope protection in industry

Flight envelope protection is currently a regular part of the flight control laws for modern fly-by-wire aircraft. However, the current types of protections differ between aircraft manufacturers, and they are static. Airbus makes use of hard limitations. This means that the aircraft system as a whole is designed with the scope of minimizing the possibility for a pilot to exceed the envelope boundaries when operating in normal law mode [6–8]. The conventional flight envelope protection setup for Airbus aircraft in normal law involves high alpha protection, load factor limitation, pitch attitude protection and bank angle protection [9]. Manual longitudinal tracking is based on the C^* criterion $C^*(t) = \frac{V}{g}\dot{\theta}(t) + n_{z_{\text{pilot}}}(t)$, which involves the load factor at pilot's station $n_{z_{\text{pilot}}}$ (more detail is given in Sec. IV.D) [10, 11]. In Airbus designs this load factor is limited between minimum and maximum values $\Delta n_{z_{\min}} \leq \Delta n_z \leq \Delta n_{z_{\max}}$. In a clean configuration (flaps, slats and gear retracted), $\Delta n_{z_{\min}} = -1g$ and $\Delta n_{z_{\max}} = 2.5g$. Moreover, the pitch attitude angle θ is limited between $\theta_{\min} = -15°$ and $\theta_{\max} = 30°$. When the angle of attack α exceeds the protection threshold α_{prot}, manual longitudinal tracking becomes proportional to the angle of attack $\alpha \sim \delta_c$ up to the maximum value $\alpha_{\max}$. This is a hard predefined limit which depends on the configuration (a.o. flap and slat setting). There are also overspeed protections (forced pitch up load factor demand near the maximum operating speed or Mach number V_{MO}/M_{MO}, which cannot be overridden manually), and low energy warnings. An overview of the types of the different protections is given in Table 1.

Table 1. Overview of current state of the art types of protections for Airbus aircraft

Mode	Type of protection				
	Display	Aural	Command limit	FCL action	Haptics
Angle of attack / low speed	Speed tape	yes	AoA mode	Apply thrust	none
Highspeed	Speed tape	yes	none	Pitch up	none
Load factor	none	none	Pilot input	none	none
Pitch angle	PFD	none	Pilot input	none	none
Roll angle	PFD	none	Pilot input	Bank command beyond 35 deg.	none
Low energy	none	yes	none	none	none

For banking, a rate control attitude hold law has been implemented for bank angles up to 33°. Beyond this threshold, the law switches into a pure bank angle control law up to the maximum value of $\phi_{\max} = 67°$. In alternate law, alpha and bank angle protections are lost. Only load factor limitation remains active, in a similar way as in normal law. The envelope boundaries for $\alpha_{\max}$, $n_{z_{\min/\max}}$, $\theta_{\min/\max}$ and $\phi_{\max}$ are static and do not take into account malfunctions or impairment, e.g. icing. Boeing has a similar setup for flight

envelope protections (bank angle protection, stall and overspeed protection), but prefers soft protections, in contrast to Airbus. These deter pilot inputs from exceeding certain predefined limits but do not prohibit them. This means that by applying a force on the controls higher than the mechanized envelope protection inceptor detent, the pilot can fly the aircraft beyond the limits of the target protected envelope, when judged to be necessary [12]. Other flight envelope protection functions have been applied by other civil aircraft manufacturers such as Embraer as well as in military jet aircraft such as the Eurofighter Typhoon [13]. Given the availability of an updated safe flight envelope, it is possible to make these limitations $\alpha_{\max}$, $n_{z_{\min/\max}}$, $\theta_{\min/\max}$ and $\phi_{\max}$ adaptive so that they closely match the actual updated envelope boundaries. As an example, in a low speed flight condition with ice accretion on the wings affecting the lift capability, the actual true stall angle of attack α_{stall} and stall bank angle ϕ_{stall} will be significantly lower than the static predefined values $\alpha_{\max}$ and $\phi_{\max}$ which are based on a nominal aircraft configuration. Lambregts discusses Envelope Protection (EP) design requirements, as well as functional, safety and performance objectives and design guidelines [14].

B.   Previous research in adaptive flight envelope protection

A variety of methods for tackling this challenge have been investigated in previous studies. In [15], online learning neural networks are used to approximate selected aircraft dynamics which are then inverted to estimate command margins for limit avoidance. The goal of the approach in [16,17] is to provide the pilot aural, visual, and tactile cues focused on maintaining the pilot's control action within predicted loss-of-control boundaries. This predictive architecture combines quantitative loss-of-control boundaries, an adaptive prediction method to estimate in real-time Markov model parameters and associated stability margins, and a real-time data-based predictive control margins estimation algorithm. This research culminated in piloted simulator evaluations in the Vertical Motion Simulator VMS at NASA Ames Research Center. Ref. [18] focuses on a flight envelope protection system for small aircraft, to allow carefree maneuvering for the less experienced pilot. Preliminary results are obtained from an empirical comparison study in the time domain, between a PID based control limiting approach, a command limiting approach and a constrained Flight Control Law (FCL) approach using Model-based Predictive Control (MPC), with and without parametric model uncertainties. In [19], an adaptive limit avoidance system is applied to provide angle of attack and load factor protection. Ref. [20] presents a dynamic flight envelope protection system for NASAs Transport Class Model. The developed protection scheme is based on a command-limiting approach that accounts for aircraft adverse aerodynamics, unusual attitude, and structural integrity, and is implemented around a standard gain-scheduled flight control law. The scheme also includes an energy protection scheme, which relies on an automatic throttle control system that implements a total energy control law. In [21], an application is presented of controller synthesis for hybrid systems to aerodynamic envelope protection and safe switching between flight modes. Each flight mode, which describes a configuration of the dynamic equations describing the motion of the aircraft, is treated as a discrete state with associated continuous, nonlinear dynamics and the safe subset of the state space (which ensures aerodynamic envelope protection) is calculated for each discrete state. Finally, Ref. [22] focuses on partial envelope protection specifically with respect to control saturation. Here, a pseudo control hedging algorithm adapts the reference model for the system output in case of unachievable commands due to control input saturation.

C.   Goal and structure

This paper focuses on using a physical approach for the definition of the flight envelope and relying on a modular control architecture involving separate pilot command filtering, which is particularly well suited to incorporate these adaptive envelope protections. Moreover, this more transparent approach allows interpreting data in each step, and it is assumed that these physical models based on flight dynamics theory will therefore facilitate certification for possible future real life applications.

The structure of this paper is as follows. An introductory global overview and a short description of the simulation model are given in Sec. II and III. Sec. IV gives a brief overview of the longitudinal manual flight control laws. The actual algorithms calculating the flight envelope boundaries are discussed in detail

in Sec. V. The implementation of these protections in the augmented control laws architecture and some desktop simulation experiments, illustrating how the protections work, are included in Sec. VI and VII. The experiment method is described in Sec. VIII. Sec. IX discusses the results. Conclusions can be found in Sec. X.

II.   Global overview

The role that envelope protection plays in the global augmented closed loop setup is illustrated in Fig. 1. Fault Detection and Diagnosis (FDD) of control system and sensor faults allows to reconfigure the control allocation algorithm if necessary. This has been investigated in the ADDSAFE project [23]. In parallel, an envelope estimation algorithm estimates the safe flight envelope boundaries [4,5]. These are calculated with respect to true airspeed V_{TAS}, flight path angle γ and bank angle ϕ. FDD as well as envelope estimation provide information to the envelope protection algorithm, which translates this information in command limiting and implements adaptive protections on the load factor n_z, the attitude angles ϕ and θ and the angle of attack α. Besides command limiting in the control laws, this envelope information can also be included in the displays and presented to the crew through haptic feedback on the pilot controls. This paper will focus specifically on envelope protection.
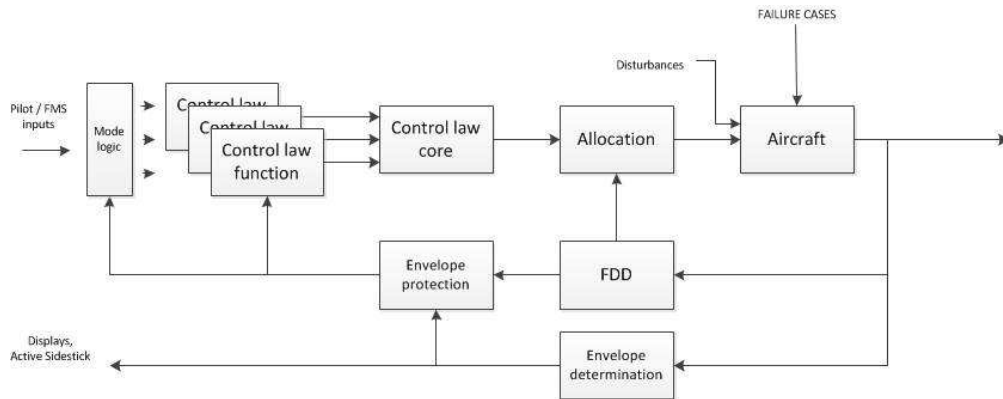

Figure 1. Global overview of envelope protection in the augmented closed loop architecture

III.   Simulation model

The model used for this research project represents an aircraft that closely resembles an Airbus A320, both in geometry as well as flight performance. As no propulsion and aerodynamic models were available, these were re-computed by means of numerical methods. The aerodynamic model was computed using the panel method as implemented in VSaero [24]. The application rule for the lift coefficients reads as follows:

$$C_L = C_{L_{\text{static}}}(\alpha, \beta, M, Re, \delta_{\text{controls}}) + C_{L_q}(\alpha, \beta, M, Re)\frac{q\bar{c}}{V} \tag{1}$$

where α and β are the angles of attack and side slip, M is the Mach number, Re the Reynolds number, δ_{controls} represents all control surface deflections (flaps, ailerons, elevator, etc.), $\bar{c}$ mean aerodynamic chord, V the true airspeed, and q the pitch rate around the body Y-axis. Application rules for the other force and moment coefficients have a similar structure.

Since the panel method does not address stall phenomena, the lift curve $C_{L_{\text{static}}}$ is adapted such that it has a maximum at the stall angle of attack by means of a parabolic approximation. The maximum angles of attack have been iterated such that the model stalls at the same speeds as the Airbus A320 at identical weights and high-lift configurations.

The weight and balance model is estimated taking structural weights, equipment, payload and fuel into account. For this project, a mean center of gravity location of 31% was used.

Model inputs include cockpit controls, combined controls (e.q. ailerons, elevators), as well as individual control surface deflections. Furthermore, steady wind and turbulence models based on the Dryden spectra have been implemented. Model outputs include basic models of sensors, such as inertial reference and air data systems, as well as internal variables for analysis purposes.

The model has been integrated in Modelica using a dedicated flight dynamics library [25]. From this implementation, a 6-DOF simulation model was automatically generated for use in Matlab/Simulink. In addition, by appropriately reversing the model inputs and outputs, Nonlinear Dynamics Inversion control laws were automatically generated to serve as a core of the flight control laws. Integration in the flight simulator was done by means of the Functional Mockup Interface (FMI) standard [26].

IV.   Manual flight control laws

The manual flight control laws are based on nonlinear dynamic inversion (NDI), combined with linear controllers, reference models and pilot command filtering as described in Ref. [27]. The longitudinal control law is somewhat different than the setup as described in Ref. [27], because it has been extended to a C^* control law.

The overall controller structure exists of four major modules, namely pilot command for roll and yaw, a C^* control law for pitch, a reference model and the actual controller, which consists of a linear controller and the actual nonlinear dynamic inversion module, as illustrated in Fig. 2. The envelope protection feature interacts with pilot command, reference model and C^* control law and will be discussed in detail in Sec. VI.A.

Figure 2. Global overview of manual control structure

A.   Nonlinear Dynamic Inversion

By making use of Nonlinear Dynamic Inversion (NDI), the nonlinear aircraft dynamics can be cancelled out such that the resulting system behaves like a pure single r-th order integrator. In Fig. 3, model inversion makes use of the airframe/engine model and control allocation relies on the so-called effector blending model. Note that the effector blending model needs to be inverted for this purpose. More detailed information is available in Ref. [27]. It should be noted that this dynamic inversion is not perfect due to the presence of the multiplicative uncertainties in the aerodynamic model. However, the linear controller has shown to be capable to deal with these modeling errors, as discussed in Ref. [27].

B.   Linear controllers

Because of the relative degree, the linear controllers work up to the second order time derivative, and they have the following control laws:

$$\nu_p = \left(K_\phi + \frac{K_{\phi_I}}{s}\right)(\phi_c - \phi) + K_{\dot\phi}\left(\dot\phi_c - \dot\phi\right) + K_{\ddot\phi}\left(\ddot\phi_c\right) \tag{2}$$

$$\nu_q = K_{\dot\theta}\left(\dot\theta_c - \dot\theta\right) + K_{\ddot\theta}\left(\ddot\theta_c\right) \tag{3}$$

$$\nu_r = \dot r_{\mathrm{comm}} = K_r\left(r_{\mathrm{comm}} - r\right) \tag{4}$$

The implementation of this setup results in the global control structure overview as presented in Fig. 3.
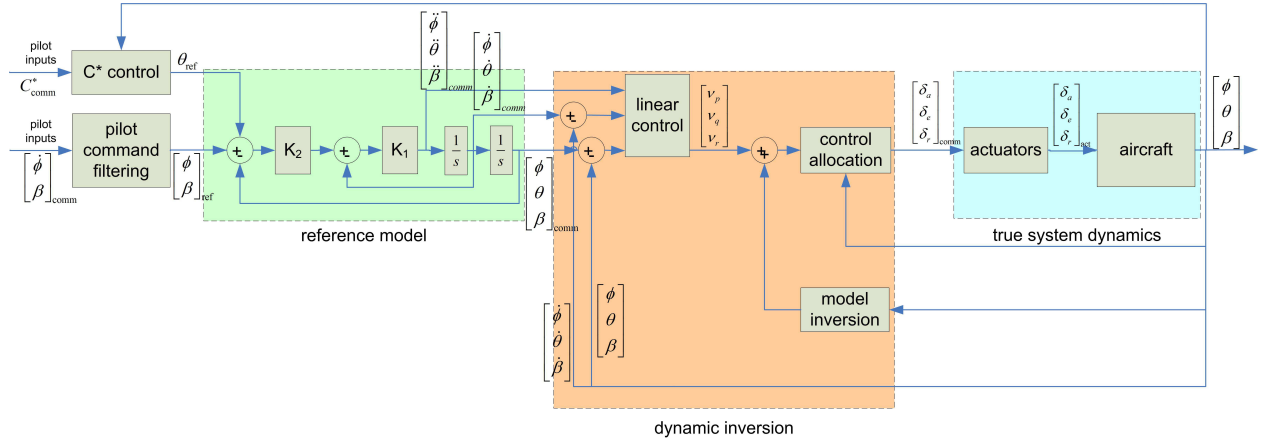

Figure 3. Global overview of the control structure seteup, with nonlinear dynamic inversion, linear controllers, reference models and pilot command filtering, modified from Ref. [27]

In Fig. 3, it can also be seen that the linear control input is based upon two orders of derivatives of the reference model, as is also described in Eq. (2) till (4).

For the yaw channel, sideslip β control has been implemented as outer loop over rate control according to the following law:

$$r_{\mathrm{comm}} = \frac{1}{V}\left(wp - A_y\right) - \left(\frac{1}{s}K_{\beta_I}\left(\beta_c - \beta\right) - K_\beta\beta\right) \tag{5}$$

C.   Pilot command module and reference model

In the pilot command module for roll, a blend is created between a rate control attitude hold (RCAH) and a pure attitude control (AC) setup. RCAH applies in the range $|\phi| \le 30°$. For $30° \le |\phi| \le 60°$, attitude control governs. This blending prevents too violent effects when reaching roll limits. From this module, the commanded angle as well as its time derivative are fed to the reference model. This is a conventional second order reference model. A more detailed overview of the setup of command module and reference model is shown in fig. 4.

Inside the pilot roll command module, the attitude control part, which acts in the ranges $30° \le |\phi| \le 60°$, must be scaled by the gain K_2^{-1} in order to guarantee a smooth fit and transition between RCAH and AC. Moreover, the dashed line in the command filtering block illustrates the switching based upon integrator saturation. Without saturation, attitude control is switched off and rate feedforward is on. As soon as the integrator saturates, the rate feedforward is switched off and the attitude control loop augments the saturated integrated output directly.
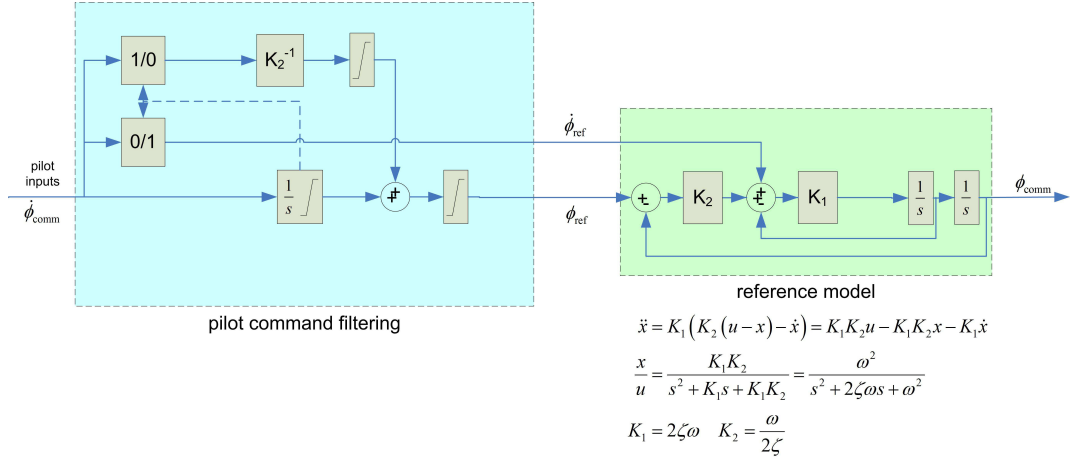
The reference model equations shown in the figure:

$$\ddot{x} = K_1 \left(K_2 \left(u - x \right) - \dot{x} \right) = K_1 K_2 u - K_1 K_2 x - K_1 \dot{x}$$

$$\frac{x}{u} = \frac{K_1 K_2}{s^2 + K_1 s + K_1 K_2} = \frac{\omega^2}{s^2 + 2\zeta\omega s + \omega^2}$$

$$K_1 = 2\zeta\omega \quad K_2 = \frac{\omega}{2\zeta}$$

Figure 4. Set up of pilot command and reference model

D. C^* longitudinal control law

A C^* control law has been implemented for longitudinal control [10, 11]. When the angle of attack α exceeds the protection threshold α_{prot}[a], the commanded angle of attack becomes proportional to the inceptor deflection $\alpha_{\mathrm{comm}} \propto \delta_c$ up to the maximum value α_{max}.

The $C^*(t)$ control signal is a weighted combination of load factor at the pilot station $n_{z_{\mathrm{pilot}}}$ and pitch rate $\dot{\theta}$ [10, 11]:

$$C^*(t) = \frac{V}{g}\dot{\theta}(t) + n_{z_{\mathrm{pilot}}}(t) \tag{6}$$

where the change in the load factor at the pilot station $\Delta n_{z_{\mathrm{pilot}}}(t)$ is calculated as follows:

$$\Delta n_{z_{\mathrm{pilot}}}(t) = \frac{V}{g}\dot{\gamma}(t) + \frac{x_a}{g}\dot{q}(t) \tag{7}$$

where the first term reflects load factor contributions from flight path changes, and the second term is the induced load factor at the pilot's seat, which depends on the distance to the center of gravity x_a. It is assumed that the pitch acceleration $\dot{q}$ and the rate of change of the flight path angle $\dot{\gamma}$ are provided by the on-board signal processing of a state-of-the-art airliner.

The practical implementation of the $C^*(t)$ control signal in the longitudinal control law is illustrated in Fig. 5. The factor $\frac{\cos\theta}{\cos\phi}$ compensates for the lift in turns and reduces the achievable load factor for higher
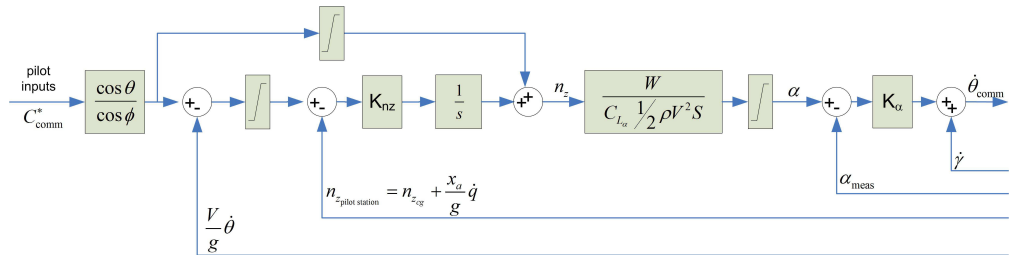

Figure 5. Control setup of the C^*/n_z control law, modified from Ref. [10]

[a]Which is in this specific context defined as: $\alpha_{\mathrm{prot}} = \alpha_{\mathrm{max}} - 2°$

pitch attitude angles. Furthermore the commanded load factor is limited as explained in Sec. I. It can be seen that the commanded $C^*(t)$ is translated in a commanded load factor $n_z(t)$. This signal is then used to calculate the commanded angle of attack as follows:

$$\alpha_{\text{comm}} = \frac{W}{C_{L_\alpha} 1/2\rho V^2 S} n_{z_{\text{comm}}} \tag{8}$$

This commanded angle of attack is then used to calculate the commanded pitch rate $\dot{\theta}_{\text{comm}}$, which is fed to the regular reference model and nonlinear controller as shown in Fig. 3 and explained in Ref. [27].

V.   Flight envelope protection algorithms

Based on the flight performance and dynamics, it is possible to calculate on-line in flight the envelope protection bounds for the maximum bank angle $\phi_{\max}$, the minimum calibrated airspeed $V_{\text{CAS}_{\min}}$, the maximum load factor $\Delta n_{z_{\max}} = n_{z_{\max}} - 1$, the minimum and maximum flight path angles $\gamma_{\min/\max}$, and the minimum and maximum pitch attitude angles $\theta_{\min/\max}$. This section will elaborate on the calculation procedure for each quantity.

A.   Minimum calibrated airspeed

Considering the standard lift equation [28]:

$$L = C_L \frac{1}{2}\rho V^2 S \tag{9}$$

where the lift coefficient before stall can be described as: $C_L(\alpha, M, Re, \delta_{\text{fl}}, \delta_{\text{sp}}) = C_{L_0}(M, Re, \delta_{\text{fl}}, \delta_{\text{sp}}) + C_{L_\alpha}(M, Re, \delta_{\text{fl}}, \delta_{\text{sp}})\alpha$. The lift coefficient C_L is affine in α, where both aerodynamic derivatives depend on Mach number M, Reynolds number Re, flap setting δ_{fl} and spoiler deflection δ_{sp}. The normal load factor n_z is defined as the ratio of lift L over weight W:

$$n_z = \frac{L}{W} \tag{10}$$

Combining Eq. (9) and (10) can be used for calculating the minimum calibrated airspeed $V_{\text{CAS}_{\min}}$ as follows:

$$V_{\text{CAS}_{\min}} = \sqrt{\frac{2n_z W}{(C_{L_{\max}} - \Delta_{C_{L_{\max}}})\rho_0 S}} \tag{11}$$

where $C_{L_{\max}} = C_{L_0} + C_{L_\alpha}\alpha_{\max}$. $\Delta_{C_{L_{\max}}}$ represents the maximum deviation with respect to the maximum lift coefficient for the purpose of robustness. These deviations are caused by uncertainties, attributed to inaccuracies in the estimated values or production tolerances. In this calculation the current values for load factor n_z and weight W are used as provided by the accelerometers and the flight management system (FMS) respectively. The up-to-date values for C_{L_0} and C_{L_α} are provided by the identification algorithm, as well as the maximum angle of attack $\alpha_{\max}$.

Similarly, one can calculate the alpha protection speed $V_{\text{CAS}_{\alpha_{\text{prot}}}}$, which represents the speed corresponding to the maximum angle of attack at which alpha protection becomes active:

$$V_{\text{CAS}_{\alpha_{\text{prot}}}} = \sqrt{\frac{2n_z W}{\left(C_{L_{\alpha_{\text{prot}}}} - \Delta_{C_{L_{\alpha_{\text{prot}}}}}\right)\rho_0 S}} \tag{12}$$

where $C_{L_{\alpha_{\text{prot}}}} = C_{L_0} + C_{L_\alpha}\alpha_{\text{prot}}$. Typically, the maximum angle of attack at which alpha protection becomes active is defined as: $\alpha_{\text{prot}} = \alpha_{\max} - 2°$.

B.   Maximum load factor and maximum bank angle

Considering the equation of motion in the aerodynamic reference frame (wind axes):

$$F_{A_Z} \cos\phi + F_{A_Y} \sin\phi + W \cos\gamma = -mV\dot{\gamma} \tag{13}$$

where the aerodynamic forces are defined as the vertical component $F_{A_Z} = -T\cos\beta\sin\alpha - L\,(V,\alpha)$ and the lateral component $F_{A_Y} = T\sin\beta + Y_{\text{aero}}\,(V,\beta)$. T represents engine thrust here. Implementing the aerodynamic forces in the kinematic equation for small sideslip angle β results in:

$$(-T\sin\alpha - L\,(V,\alpha))\cos\phi + Wn_Y\sin\phi + W\cos\gamma = -mV\dot{\gamma} = -W\Delta n_{z_{\text{comm}}} = -W\,(n_{z_{\text{comm}}} - 1) \tag{14}$$

Eq. (14) can be used for calculating the maximum commanded load factor $\Delta n_{z_{\max}}$ as well as for the maximum bank angle $\phi_{\max}$. The maximum commanded load factor is calculated as follows:

$$\Delta n_{z_{\max}} = \frac{(C_{L_{\max}} - \Delta_{C_{L_{\max}}})\bar{q}S}{W}\cos\phi - n_Y\sin\phi - cos\gamma + \frac{T}{W}\sin\alpha\cos\phi \tag{15}$$

Rewriting Eq. (14) for bank angle ϕ, while assuming that the term $Wn_Y\sin\phi \approx 0$ will be small compared to the other terms:

$$\cos\phi = \frac{m\,(g\cos\gamma + V\dot{\gamma})}{T\sin\alpha + L\,(V,\alpha)} \tag{16}$$

For extreme bank angles the following relationship can be derived:

$$\phi_{\max} = \pm\arccos\left(\frac{m\,(g\cos\gamma + V\dot{\gamma})}{T\sin\alpha + (C_{L_{\max}} - \Delta_{C_{L_{\max}}})\tfrac{1}{2}\rho V^2 S}\right) \tag{17}$$

In Eqs. (15) and (17), $\Delta_{C_{L_{\max}}}$ represents the maximum deviation with respect to the maximum lift coefficient for the purpose of robustness. In these calculations the current values for airspeed V and its derivative $\dot{V}$, Thrust T, angle of attack α and flight path angle γ are used. For normal maneuvers of a conventional civil airliner, the maximum bank angle is not expected to exceed $35°$.

Reducing speed will restrict the available bank range to lower values of $\pm\phi_{\max}$. At stall speed, no bank authority will be left.

C.   Minimum and maximum flight path angles

Considering the equation of motion [28]:

$$F_{A_X} - W\sin\gamma = m\dot{V} \tag{18}$$

where the forward aerodynamic force is defined as: $F_{A_X} = T\cos\beta\cos\alpha - D\,(V,\alpha)$. Implementing the aerodynamic force in the kinematic equation for small sideslip angle β and solving for the flight path angle γ results in:

$$\gamma = \arcsin\left(\frac{T\cos\alpha - D\,(V,\alpha) - m\dot{V}}{W}\right), \qquad \text{with:} \tag{19}$$

$$D\,(V,\alpha) = \bar{q}S\left(C_{D_0} + C_{D_\alpha}\alpha + C_{D_{\alpha^2}}\alpha^2\right) \tag{20}$$

The minimum and maximum flight path angles are then defined as:

$$\gamma_{\min} = \arcsin\left(\frac{(T\cos\alpha - D\,(V,\alpha))_{\min} - m\dot{V}}{W}\right) \tag{21}$$

$$= \arcsin\left(\frac{T_{\min}\cos\alpha - (C_{D_{\max}} - \Delta_{C_{D_{\max}}})\tfrac{1}{2}\rho V^2 S}{W} - \frac{\dot{V}}{g}\right) \tag{22}$$

$$\gamma_{\max} = \arcsin\left(\frac{(T\cos\alpha - D(V,\alpha))_{\max} - m\dot{V}}{W}\right) \tag{23}$$

$$= \arcsin\left(\frac{T_{\max}\cos\alpha - \left(C_{D_{\min}} + \Delta_{C_{D_{\min}}}\right)\frac{1}{2}\rho V^2 S}{W} - \frac{\dot{V}}{g}\right) \tag{24}$$

where the term $m\dot{V}$ reflects the impact of acceleration or deceleration on the reachable flight path angles. In the simulator experiments described in Ref. [5], it has been observed that the impact of acceleration on the reachable flight path angles during a go around maneuver was significant. Moreover $\Delta_{C_{D_{\max}}}$ and $\Delta_{C_{D_{\min}}}$ represent the maximum deviation with respect to the maximum and minimum drag coefficient for the purpose of robustness. In case of windshear, these equations need to be extended by a so-called $F-$factor in a similar way as the speed rate of change $\dot{V}$ in Eq. (22) and (24) [29, 30]:

$$\gamma \approx \arcsin\left(\frac{T - D}{W} - F\right) \tag{25}$$

where the $F-$factor reflects the speed rate of change $\dot{V}$, caused by the windshear components. For flight path angles $\gamma < 35°$, it can be stated that:

$$F \approx \frac{\dot{W}_x}{g} + \frac{\dot{W}_h}{g}\sin\gamma - \frac{W_h}{V} \tag{26}$$

where W_x is the frontal wind component and W_h is the vertical wind component. In the context of envelope protection, these gusts must be estimated in real time. In this project, it is assumed that these measurements are available. This can be done by means of Lidar-measurements for example. Substituting Eq. (26) in Eq. (25) and rewriting for the flight path angle results in a new expression:

$$\gamma \approx \arcsin\left(\left(1 + \frac{\dot{W}_h}{g}\right)^{-1}\left(\frac{T - D}{W} - \frac{\dot{W}_x}{g} + \frac{W_h}{V}\right)\right) \tag{27}$$

D.   Minimum and maximum pitch attitude angles

The minimum and maximum pitch attitude angles are calculated by means of the previously calculated limits:

$$\theta_{\max} \approx \gamma_{\text{current}} + \alpha_{\max} \tag{28}$$

$$\theta_{\min} \approx \gamma_{\min} \tag{29}$$

VI.   Implementation of the protections in the augmented flight control laws architecture

The different protections, for which the bounds have been calculated in Sec. V, can be implemented in three different augmentation loop closure channels, as illustrated in Tab. 2. Relevant bounds can be implemented in the flight control law. Especially the control architecture involving separate pilot command filtering is particularly well suited to incorporate these adaptive protections. Besides, envelope bound information can also be displayed in the primary flight display (PFD), in a similar way as was described in Ref. [4, 5]. As a third channel of information, haptic feedback can be provided on the pilot's stick. As a result, this approach is a combined *hard* (protections in controllers) and *soft* (haptic feedback on stick) adaptive envelope protection.

Table 2. Overview of types of protections for the new setup

Mode	Type of protection				
	Display	Aural	Command limit	FCL action	Haptics
Angle of attack / low speed	Speed tape	yes	AoA mode	Apply thrust	yes
Highspeed	Speed tape	yes	none	Pitch up	none
Load factor	none	none	Pilot input	none	yes
Pitch angle	(PFD)	none	Pilot input	none	yes
Roll angle	PFD	none	Pilot input	Bank command beyond 35 deg.	future work
Low energy	none	yes	none	none	none
Vertical speed	v/s tape	none	none	none	none

A. Flight control laws

The protections for load factor and angle of attack have been implemented in the longitudinal manual control laws as shown in Fig. 6. This figure builds further upon the manual flight control law setup as discussed previously in Sec. IV and Fig. 5. The previously static saturation blocks for n_z and α have been made adaptive.
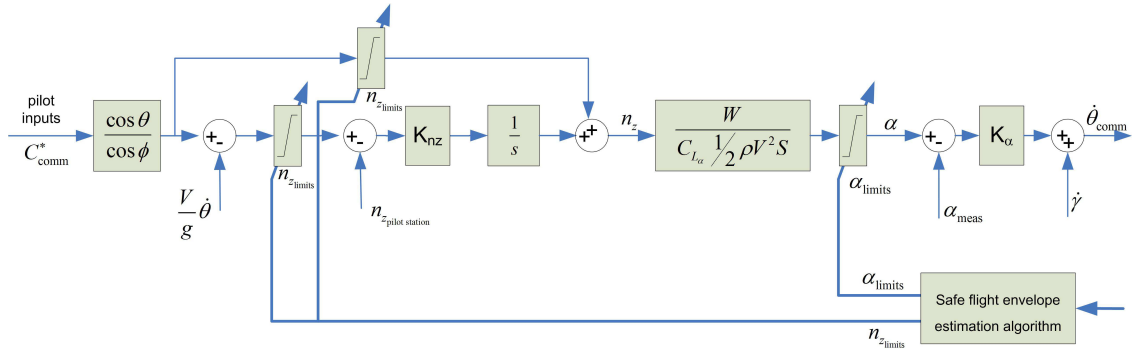

Figure 6. Longitudinal control law setup with adaptive envelope limits

The protections for bank angle have been implemented in the lateral manual control laws, as illustrated in Fig. 7.

The roll angle limitations act only on the attitude control (AC) part of the pilot command setup. This means that $|\phi| = 30°$ of bank angle is attainable in every scenario, also if this would make the aircraft stall. Consistently with the pilot command limitation, a similar limitation has been implemented in the reference module.

B. Cockpit displays

Part of the information obtained from the envelope estimation algorithm can also be presented to the pilots. This is done in the primary flight display (PFD). The speed and flight path angle boundaries, which apply for the current bank angle and sideslip angle, are shown on the relevant parts of the PFD. Also the bank angle limits are displayed on the PFD.
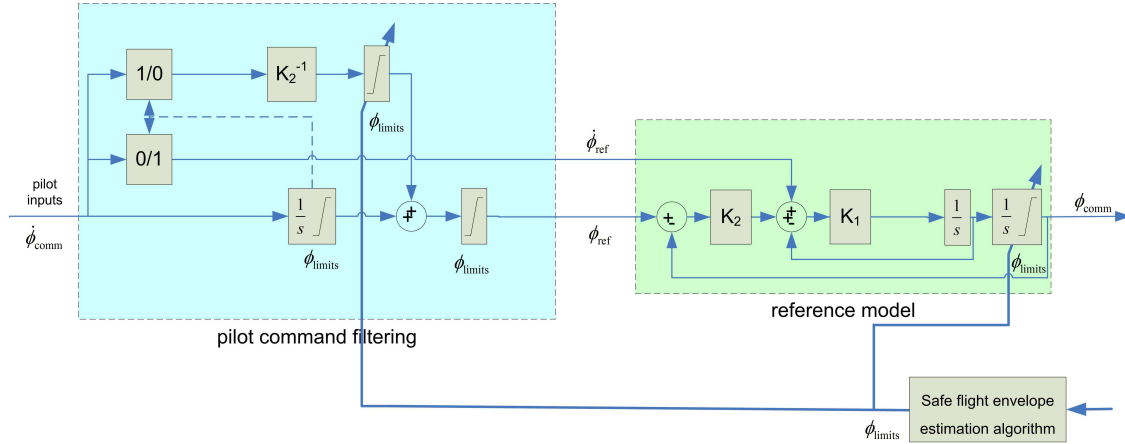
Figure 7. Directional control law setup (pilot command and reference model) with adaptive envelope limits

The minimum calibrated airspeed (CAS), calculated in Sec. A, is presented on the speedtape at the left hand side of the artificial horizon in the PFD. The flight path angle information γ, calculated in Sec. V.C is translated into vertical speed $\dot{h}$ and presented on the vertical speed tape at the right hand side of the artificial horizon in the PFD. Safe envelope information presented on the vertical speed tape, as illustrated in Fig. 8, is absent in current PFDs. In this new setup, these amber lines mark the vertical speed ranges where no equilibrium can be established. In practice, this means that speed will increase in the lower amber region, even for idle thrust, and that speed will decrease in the upper amber region, even with full thrust. For the bank angle limits, the red regions indicate where stall will occur and are determined by the maximum bank angle as calculated in Sec. V.B.
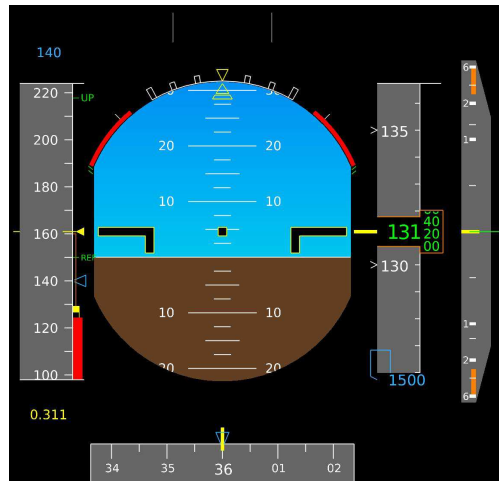

Figure 8. Primary Flight Display with envelope boundary information for airspeed (left, non-adaptive in conventional displays), bank angle (top, new) and vertical speed (right, new)

C.   Haptic feedback

One of the potential ways to communicate the boundaries of the safe flight envelope to the cockpit crew is through haptic feedback. In the current evaluation a haptic feedback concept was incorporated that uses a combination of stick force gradient feedback and stick shaker to communicate envelope boundaries.

The haptic feedback provided in near-stall situations is divided into two categories, depending on the severity of the minimum speed incursion. Two areas are defined here, see Figure 9(a). The inner border (red dashed line) indicates the area beyond which proximity to the stall limit is communicated by a smoothly increased stiffness on the stick, the effect of which is illustrated in Figure 9(b). This stiffness increase is proportional to the magnitude of the incursion of the red alerting margin in Figure 9(a). When speed is reduced beyond the second border, (blue dashed line in Figure 9(a)) a vibration (a.k.a. 'stick shaker) is felt on the stick. Load factor and overspeed boundaries are communicated using the same method of stiffness feedback, but without the additional vibration cue.

To be able to translate perceived feedback into a desired action, it is required that the pilot receives the force feedback with sufficient anticipation. If for example the aircraft experiences a sudden increase in load factor while its velocity is rapidly decreasing, the stall speed might be reached very quickly. Examples of such maneuvers are a sustained pull up or a high bank angle coordinated turn. Due to the rapid increase of the stall speed caused by the fast rise in load factor, it is necessary to take into account the time the pilot needs to understand and react to the haptic feedback. To this end, predictions are made of load factor and speed, taking into account a certain cognition time. When the predicted values exceed the envelope limits, the haptic feedback boundaries (as illustrated in Figure 9(a)) are shifted inwards to match the aircrafts current velocity.
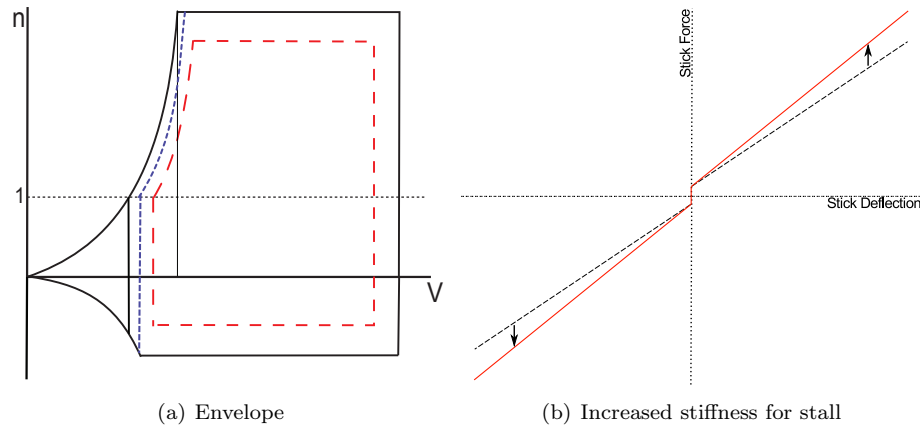

(a) Envelope

(b) Increased stiffness for stall

Figure 9. Haptic feedback properties

VII.   Desktop simulation experiments

A basic demonstration of the envelope protection concept is given in this section. This serves as an illustration of the basic functionalities, before the complete evaluation in the moving base simulator, involving more complex scenarios.

Fig. 10 illustrates the safe flight envelope bounds for a sample pitch command. After 5s from the start of the simulation, an approximately 40 KCAS airspeed reduction is commanded as an autothrottle step input as shown in Fig. 11(b); then after 11s, a longitudinal pulse is given on the control stick as shown in Fig. 11(a), together with the corresponding elevator deflection. As can be seen in the lower part of Fig. 10(a), the maximum α-limit is reached very quickly. Since the maximum allowable load factor is calculated while taking this α-limit as well as the current airspeed into account, see Sec. V.B, it can be seen that the value of the maximum load factor starts to reduce as soon as the plane starts slowing down. Consistent with the α-limit, also the commanded load factor is limited and the aircraft responds accordingly. In Fig. 10(b), in the first place the link with pitch attitude angle and calibrated airspeed can be seen. Maximum angle of attack corresponds also with maximum pitch attitude angle. However, while α is saturated, the flight path

angle γ is still building up, which contributes to the steady increase of the pitch attitude angle, see also Sec. V.D. As can be seen in Sec. V.A, the minimum calibrated airspeed is calculated based on the maximum angle of attack, and this is confirmed in Fig. 10(b). This figure also shows that the speed reduction also results in a reduced bank authority. Finally, when the maximum angle of attack is reached steadily (after the maneuver), at approx. 24s, all protection limits confirm consistency: minimum airspeed and maximum pitch attitude angle have been reached, no bank authority is left, and the flight control law starts commanding negative pitch rate, illustrated by the maximum load factor which becomes negative. Including $\Delta n_{z_{max}}$ as part of the haptic feedback would make the pilot aware of the imminent stall and the corrective maneuver which is performed automatically.
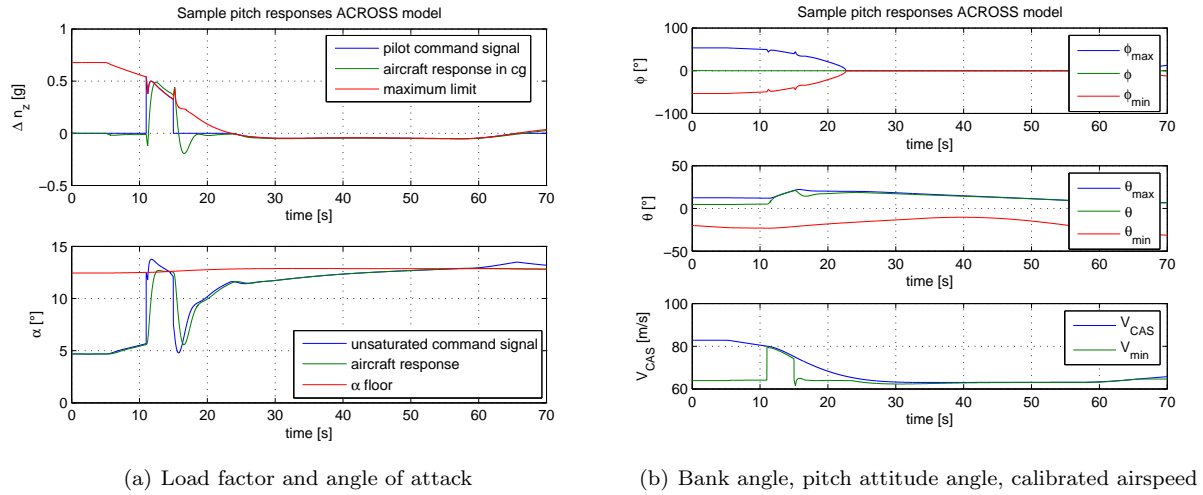

(a) Load factor and angle of attack

(b) Bank angle, pitch attitude angle, calibrated airspeed

Figure 10. Safe flight envelope bounds for sample pitch command

(a) Commanded load factor and elevator deflection
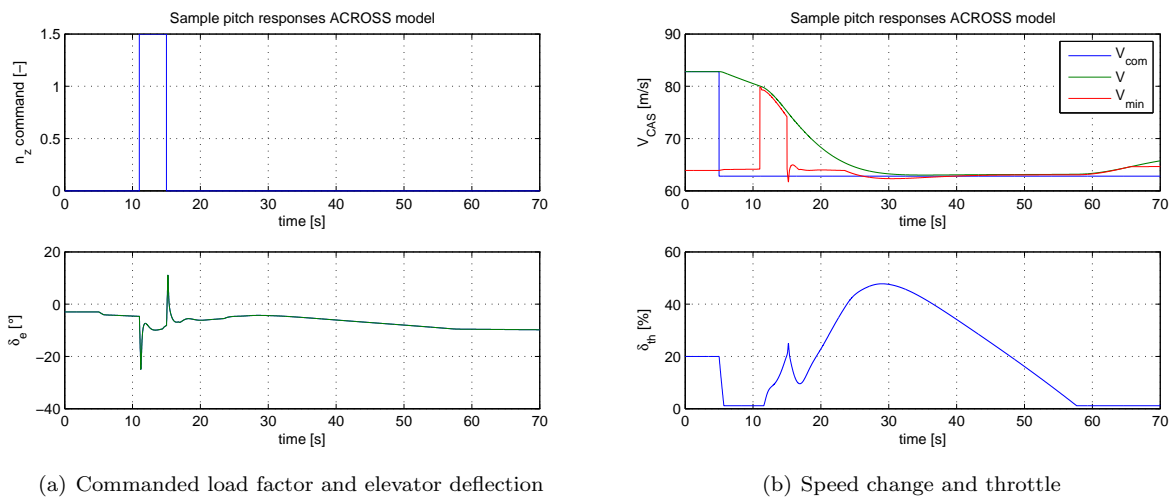
(b) Speed change and throttle

Figure 11. Commands and control effector behavior for sample pitch command

The evolution of the safe flight envelope bounds for a speed reduction of 20 m/s ($\sim$ 40 KCAS) only, similar as before, is illustrated in Fig. 12 and 13. It can be seen in Fig. 12(a) that the angle of attack

starts to increase gradually. The maximum load factor limit is reduced accordingly, representing the reduced margin to the stall limit. At around 55s, the maximum alpha limit has been reached and correspondingly the maximum load factor starts pushing down the command signal. Fig. 12(b) shows the speed reduction, and the minimum CAS speed limit is reached consistently with maximum angle of attack. The time histories for pitch attitude angle and bank angle limits confirm the same trend: no pitch up margin or control authority are left after 55s.
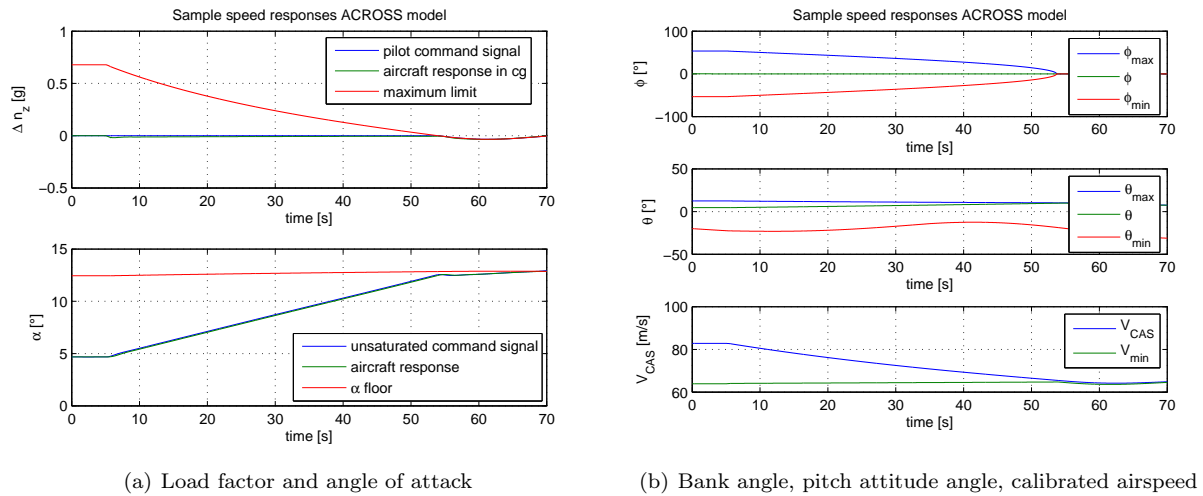

(a) Load factor and angle of attack

(b) Bank angle, pitch attitude angle, calibrated airspeed

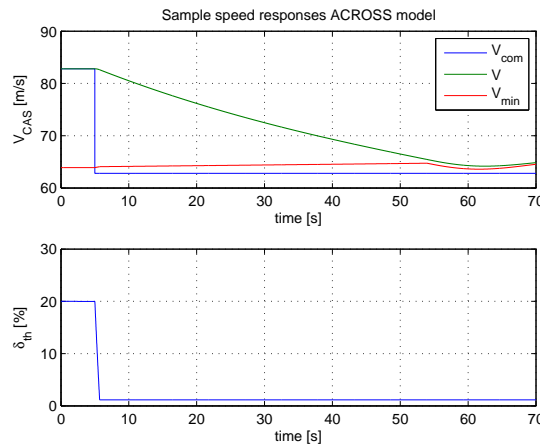**Figure 12. Safe flight envelope bounds for sample speed command**

Figure 13. Speed change and throttle behavior for sample speed command

Fig. 14 illustrates the safe flight envelope bounds for a sample roll command. After 5s from the start of the simulation, a 20 m/s speed drop is commanded as an autothrottle step input (see Fig. 15(b)) similarly as in the scenario before; then after 20s into the simulation run, a lateral pulse is given on the control stick, as shown in Fig. 15(a), together with the corresponding aileron deflection. It can be seen in Fig. 14(b) that the envelope protection algorithms in the control law prevent overbanking beyond the stall limits. The time dependent variation of the maximum bank angle bounds is caused by the variation in speed. In this figure, it can also be seen that the maximum pitch attitude and the minimum calibrated airspeed bounds vary

accordingly to reflect the impact of the bank angle on the longitudinal performance margin and the speed margin, as discussed in Sec. V.A. The cause of the reduced maximum pitch attitude and increased minimum airspeed is also illustrated in Fig. 14(a). An increased angle of attack is needed with non-zero bank angle, and this reduces the margins to stall. Similarly, the maximum vertical load factor limit is also scaled down, as discussed in Sec. V.B.
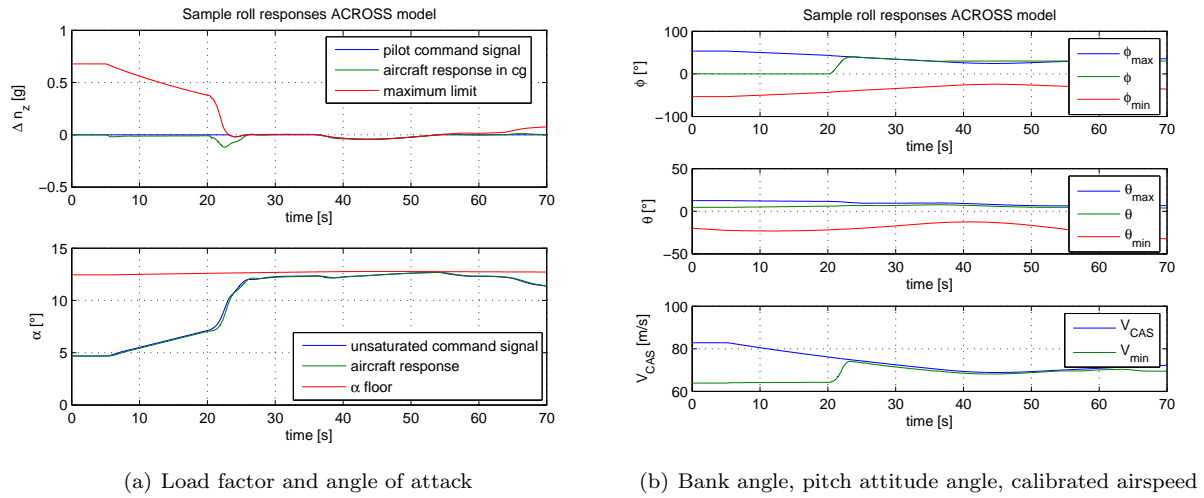

(a) Load factor and angle of attack

(b) Bank angle, pitch attitude angle, calibrated airspeed

Figure 14. Safe flight envelope bounds for sample roll command

(a) Commanded bank and aileron deflection
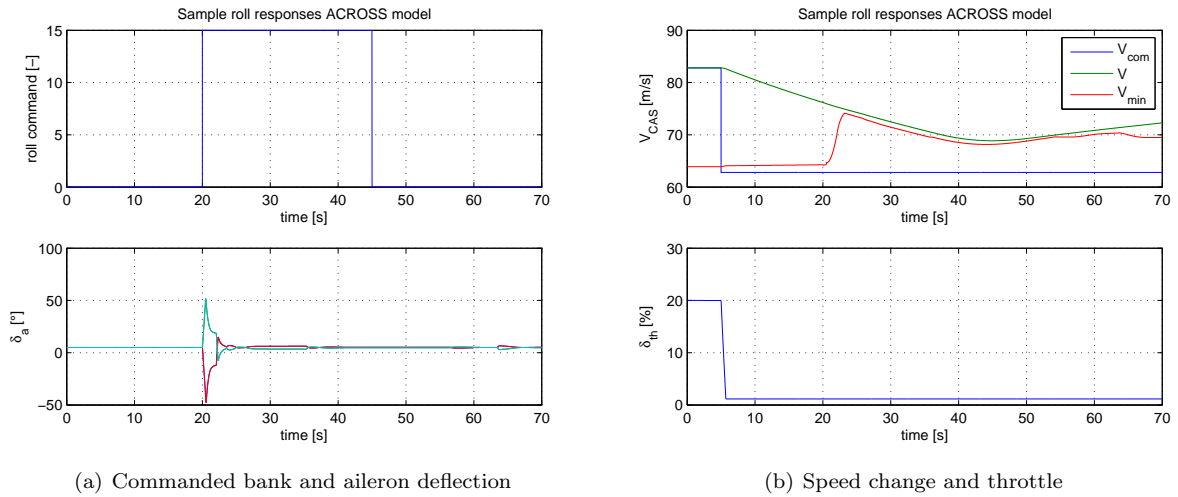
(b) Speed change and throttle

Figure 15. Commands and control effector behavior for sample roll command

Summarizing, the three test scenarios discussed here illustrate that all safe flight envelope bounds develop accordingly with maneuvers and that the different bounds are consistent. All changes can be explained from the perspective of the flight physics. The sensitivities of the boundaries for minimum airspeed, maximum bank angle and maximum load factor for deviations of 5%, 10% and 15% in the maximum lift coefficient are illustrated in Table 3 for a flight condition with airspeed 83m/s (= 160 KCAS) and altitude 4000m (= 13000ft). Table 4 shows similar results for the sensitivities of the boundaries for minimum and maximum

flight path angle for similar deviations in the minimum and maximum drag coefficient.

Table 3. Sensitivities of safe flight boundaries for uncertainties in $C_{L_{\max}}$ for a flight condition with airspeed $V_{CAS} = 83m/s$ and altitude $h = 4000m$

$\frac{\Delta C_{L_{\max}}}{C_{L_{\max}}}$	$V_{CAS_{\min}}$	$\phi_{\max}$	$\Delta n_{z_{\max}}$
0%	63.9m/s	53.44°	0.6788g
5%	65.6m/s	51.17°	0.5948g
10%	67.4m/s	48.55°	0.5108g
15%	69.3m/s	45.51°	0.4269g

Table 4. Sensitivities of safe flight boundaries for uncertainties in $C_{D_{\max/\min}}$ for a flight condition with airspeed $V_{CAS} = 83m/s$ and altitude $h = 4000m$

$\frac{\Delta C_{D_{\max/\min}}}{C_{D_{\max/\min}}}$	$\gamma_{\min}$	$\gamma_{\max}$
0%	−20°	12°
5%	−19°	11.6°
10%	−18°	11.2°
15%	−17°	10.9°

VIII. Experiment method

The method for the piloted evaluation was based on standard procedures for human factor experiments. NASA TLX workload assessment evaluations were done after each run, combined with a short situation awareness questionnaire. A more extensive questionnaire was given at the end of the study. Some procedures were shortened because of time restrictions. The number of pilots and repetitions were smaller than required for a full statistical analysis of the experiment, but are sufficient to observe certain trends.

Overall, the validation objectives were to evaluate the usability of these new systems functionalities and their possible impact on operational safety. More concretely, the aim of the experiments was to provide answers to the following three hypotheses:

1. Will adaptive flight envelope protection **prevent loss of control** and result in **reduced workload** near the edges of the flight envelope in nominal as well as in off-nominal conditions (icing, etc.) which are not taken into account in the conventional flight envelope protection?

2. Will envelope information on the displays, in combination with adaptive flight envelope protection, improve the **situational awareness** of the flight crew **about the altered flying capabilities**, caused by the off-nominal condition?

3. Will haptic feedback on the controls, in combination with adaptive flight envelope protection, improve the **situational awareness** of the flight crew **about the protective action** that the adaptive flight envelope protection is doing?

A. Technologies

The baseline condition for comparison was the conventional flight control system, which was manually flown. The controller considered in this paper is set up such that the pilot could manually maneuver the aircraft by means of the sidestick, much like the conventional manual control strategy. The perceived dynamics by the fly-by-wire (FBW) algorithm are a rate command/attitude hold scheme for C^*/n_z longitudinally and $\dot{\phi}$ laterally. The pedals steer the sideslip β directly, but were not used during the experiments. During the evaluations, the aircraft was flown in the current technology flight control system mode and in new technology mode. In the former configuration, aircraft control was achieved via the current configuration of fly-by-wire with conventional envelope protections. The latter configuration includes adaptive envelope protections, envelope information on the primary flight display, and adaptive haptic feedback on the sidestick. Two scenarios were considered in the experiments: ice accretion on the wings and windshear. These scenarios were flown in a grouped and fixed order with half of the pilots first flying with conventional technologies and the other half with the new technologies under investigation. At the start of the session the pilot was given some time to familiarize himself or herself with the simulator, experiment procedure, and rating scales.

B.   Apparatus

The evaluation was performed on the SIMONA Research Simulator (SRS) at Delft University of Technology, see Fig. 16. The SRS is a 6-DOF research flight simulator, with configurable flight deck instrumentation systems, wide-view outside visual display system, electric control loading and motion system. The middle-ware software layer called DUECA (Delft University Environment for Communication and Activation) allows rapid-access for programming of the SRS, relieving the user of taking care of the complexities of network communication, synchronization, and real-time scheduling of the different simulation modules [31].
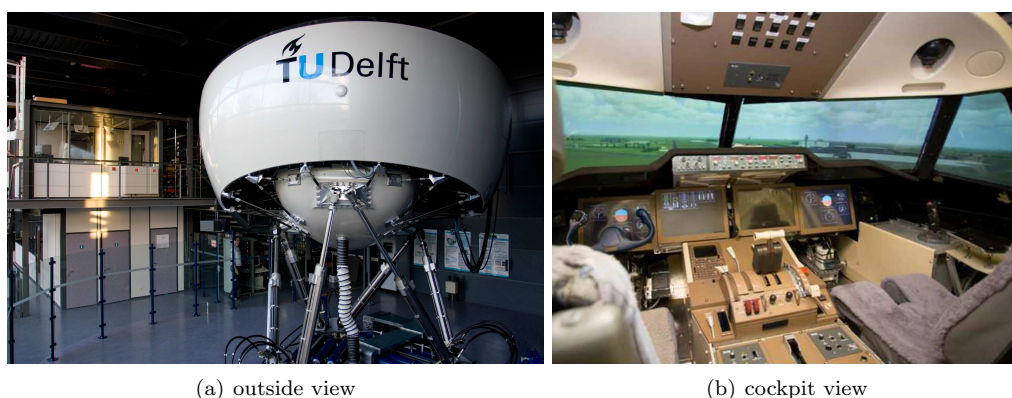

(a) outside view   (b) cockpit view

Figure 16. The SIMONA (SImulation, MOtion and NAvigation) Research Simulator (SRS) at Delft University of Technology, source: Joost Ellerbroek

1.   Flight Deck Instrumentation

The overall flight deck of the SRS was set up to resemble a simplified generic airliner cockpit. The installed hardware consisted of two aircraft seats, an electrically actuated sidestick (1st officer's position) and rudder pedals, a B777 control pedestal, 4 LCD screens to display the flight instruments (60Hz refresh rate), and a B737 mode control panel (MCP).

The displays were based on the Airbus Electronic Flight Instrumentation System (EFIS). They were shown on the LCD panels mounted in front of the pilot at the ergonomically correct locations. Not all display functionalities were incorporated, one notable omission was the Flight Director (FD), which normally gives steering commands to the pilot.

2.   Outside Visual System

The SRS has a wide field-of-view collimated outside visual system to give the pilot attitude information, as well as to induce a sense of motion through the virtual world. Three LCD projectors produce computer generated images on a rear-projection screen, which was viewed by the pilots through the collimating mirror. The resulting visual has a field of view of 180° x 40° with a resolution of 1920 x 1200 pixels per projector. Update rate of the visual was the same as the main simulation at 100 Hz, while the projector refresh rate was 120 Hz [32].

For this evaluation, visual representations of Amsterdam Airport Schiphol and Nice Airport were used. All runways and major taxiways were in their correct location, complemented with the most important buildings on the airfield. The surrounding area was kept simpler, with a textured ground plane showing a rough outline of the Mediterranean and the Dutch coast and North Sea.

C.   Participants

Familiarity with the flown aircraft is one of the main requirements for the participants in a piloted evaluation. Some flight test or evaluation experience is also beneficial, especially when using standard rating scales.

In this campaign seven professional airline pilots with an average age of 41 years and an average experience of about 9,700 flight hours, participated in the evaluation. They were all type rated for the Airbus A330 aircraft, and had experience in HQ evaluations and the rating method used. More details about the participating pilots can be found in Table 5.

Table 5. Demographic survey of participating pilots

pilot	age	total flight hours	flight hours in Airbus
pilot 1	56	10,800	4,500
pilot 2	29	1,010	310
pilot 3	41	16,700	5,900
pilot 4	47	14,500	2,500
pilot 5	37	6,000	300
pilot 6	43	12,600	1,900
pilot 7	35	6,500	1,250

D.   Measures

The impact of the new technology was assessed by means of some operational dependent measures. The operational variables were concerned with the interaction between the new technology and the pilot. Objective (for example, measured pilot control activity) as well as subjective (for example, workload assessment) operational variables were measured and compared.

1.   Objective measures

The objective measurements in the evaluation consisted of the pilot activity, measured by the RMS of the stick deflection and deflection rate, and some selected states of the aircraft, such as margin to stall angle of attack, margin to stall speed and margin to maximum bank angle.

2.   Subjective measures

Subjective measures consisted of situation awareness and workload questionnaires. The situation awareness questions focused on the perception level as described by Endsley [33]. Assessment of the workload was done by means of the NASA Task Load Index (TLX) [34].

E.   Procedure

Two scenarios have been defined with the purpose of bringing the experiment crews towards the edge of the safe flight envelope, namely an icing scenario during approach at Amsterdam Airport Schiphol in the Netherlands in freezing rain and a windshear scenario during approach towards Nice airport in South France. Both are elaborated below.

1.   Icing scenario

The geometry of the icing scenario is shown in Fig. 17. At the start of each icing run, subjects were given an ATC request to minimize speed due to traffic ahead. A northerly course is flown first, after which the centerline of runway 27 is intercepted near waypoint WP5. In the vicinity of waypoint WP3, ice accretion

is started. Ice builds up slowly on the wings, resulting in a reducing lift capability and increasing drag, combined with an earlier stall, as illustrated in Fig. 18. The gradual pace of the ice accretion in two phases is illustrated in Fig. 19, together with some significant horizontal wind gusts. It is expected that the combination of both makes it more difficult for the crew to notice the changes in the flight envelope boundaries.

The simulated wind field consists of a static wind component and a gust component:

$$W = W_{\text{st}} + W_{\text{gust}} \tag{30}$$

The static wind component W_{st} is defined as a fixed wind intensity and is estimated based on statistical data provided by the Royal Netherlands Meteorological Institute (KNMI). This wind intensity can be calculated as a function of the flight altitude h and the measured wind speed at 20m altitude W_{20m}[35]:

$$W_{\text{st}} = 0.204 W_{20m} ln \left(\frac{h + 0.15}{0.15} \right) \tag{31}$$

The second wind component in Eq. (30) is the gust component W_{gust}. A simplified version of a commonly used gust model is the 1-cosine-shaped gust expressed by Ref. [36,37]:

$$W_{\text{gust}} = \frac{W_G}{2} \left(1 - \cos \left(2\pi \, (t - t_{\text{trig}}) \, \frac{1}{T_g} \right) \right) \tag{32}$$

which depends on the maximum gust intensity W_G, simulation time t, the time instant when the gust is triggered t_{trig} and the gust duration T_g. The gust intensity W_G is estimated based on statistical data provided by the KNMI. To avoid the repetition of the same gust conditions for each experiment run, different magnitudes of gust components are utilized, assuming worst case scenarios. For this, wind gust intensities with a probability of occurrence smaller than 20% have been taken.

During ice accretion on the wings, the actual lift force is decreasing while drag is increasing. As a consequence, a larger angle of attack and/or a higher airspeed are required to compensate for the lift loss, and more thrust is needed to compensate for the drag induced speed loss. However, the maximum angle of attack decreases and stall speed increases simultaneously which reduces the margin to stall. Ice accretion is also expected to impact roll behavior significantly, but this has not been considered in this research. The expected impact is primarily on roll stability and behavior, which has consequences for the lateral control loops, but not as much for the envelope. This ice accretion phenomenon takes place between waypoints WP3 and WP4. Due to the icing effects, the turn at WP5 has to be performed cautiously, since there is a significant risk that the pilot would roll beyond the safe roll limit, where the reduced vertical lift component cannot compensate the aircraft weight anymore, and a stall would be initiated.

Purpose of the simulator experiments is to evaluate if the flight envelope estimation and protection algorithm, combined with haptic feedback on the pilot controls, provides a positive contribution in this scenario. With the new technology, the pilot will see the up-to-date minimum speed and maximum bank angles, taking into account the effects of icing. Moreover, when he approaches stall, in the alpha-protection region, he will feel the increasing stick stiffness as an addtional sensory feedback channel that he is approaching the boundaries of the safe flight envelope. Oversteering beyond the stall limit will not be possible thanks to the adaptive flight envelope protections.

2.   Windshear scenario

Windshear is characterized by strong variations of wind direction and velocity which can result from a large variety of meteorological conditions, such as topographical conditions, temperature inversions, sea breezes, frontal systems, strong surface winds and thunderstorms or rain showers, [38]. Wind shear conditions have been responsible for numerous accidents or incidents. The encounter of windshear during the takeoff, climb or approach phase is very critical. The flight crew has very little time to recognize the phenomenon and to initiate the recovery procedure. Moreover, during these flight phases the workload is already high and as a result will lead to a dangerous increase in reaction time.
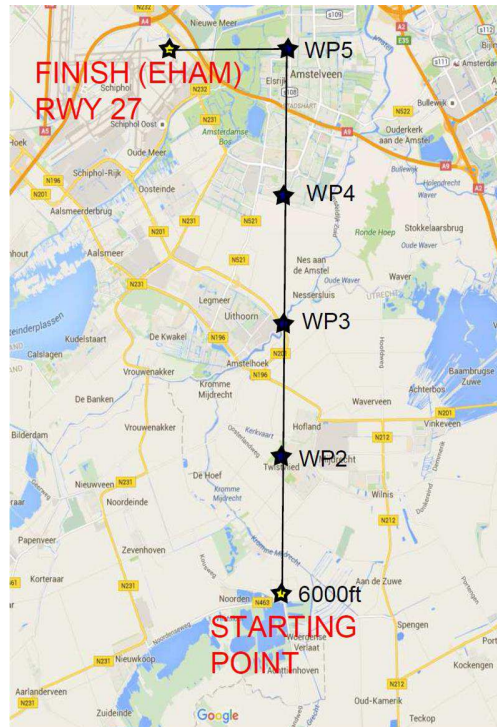
Figure 17. Flight track with waypoints towards runway 27 at Schiphol airport, source: Google Maps

This scenario takes place during final approach along the coastline of Sourth France towards runway 22 of Nice Côte d'Azur airport, as illustrated in Fig. 20. The test pilots are asked to fly over the waypoints presented in Fig. 20 while descending to 4,000 ft. Following the first three waypoints directs the aircraft to MAP22 where the visual approach to runway 22 is initiated (see upper left Jeppessen chart within Fig. 20). All these waypoints are also presented on a Navigation Display (ND) which can be zoomed in or out at the pilots discretion.

The most severe type of windshear is the one generated by convective storms such as thunderstorms. Occasionally, these may generate a rapid air mass downdraft which is also known as a microburst. These are also the most violent type of wind shear since it has caused the highest number of incidents and accidents.

The microburst's wind components are characterized by a strong downdraft from the thunderstorm which spreads out near the ground to produce a severe wind shear [39], as illustrated in Fig. 21(a). Given the location of the microburst with respect to the aircraft as indicated in Fig. 21(a), the aircraft will be pushed down by the downward vertical wind component first. The downward wind component will increase the wing's angle of attack getting closer or even surpassing their stall value. Subsequently, when flying out of the downdraft, a combined side- and tailwind will build up, which reduces the airspeed of the aircraft rapidly, provoking a significant decrease in lift force and an uncommanded pitch down motion [38–40]. The simulated wind components are illustrated in Fig. 21(b). More information about wind shear simulations can be found in Ref. [38].

In accordance with current technology, pilots get a visual and aural 'Windshear' warning as soon as it is detected by the on-board systems. The windshear recovery procedure, which is part of their training program, consists of the following steps: setting the throttle levers at TOGA (Take Off / Go Around), raising pitch attitude to 20 deg, reducing pitch if stall warning occurs, closely monitoring flight path and shear, smooth recovery to normal climb once out of shear. The main contribution from the adaptive envelope protections is expected for the steady state vertical speed limits, which are calculated taking into account the wind effects. As such, the pilot can observe what his maximum sustained climb rate is at every time
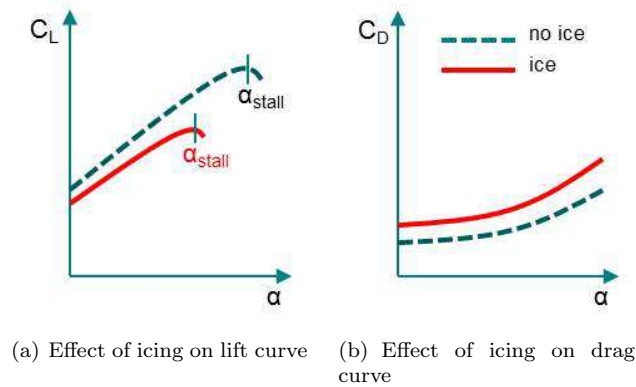
(a) Effect of icing on lift curve

(b) Effect of icing on drag curve

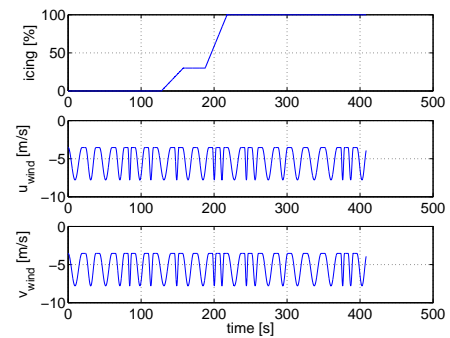**Figure 18. Sketch of the icing characteristics**

Figure 19. Icing progress and wind gust conditions
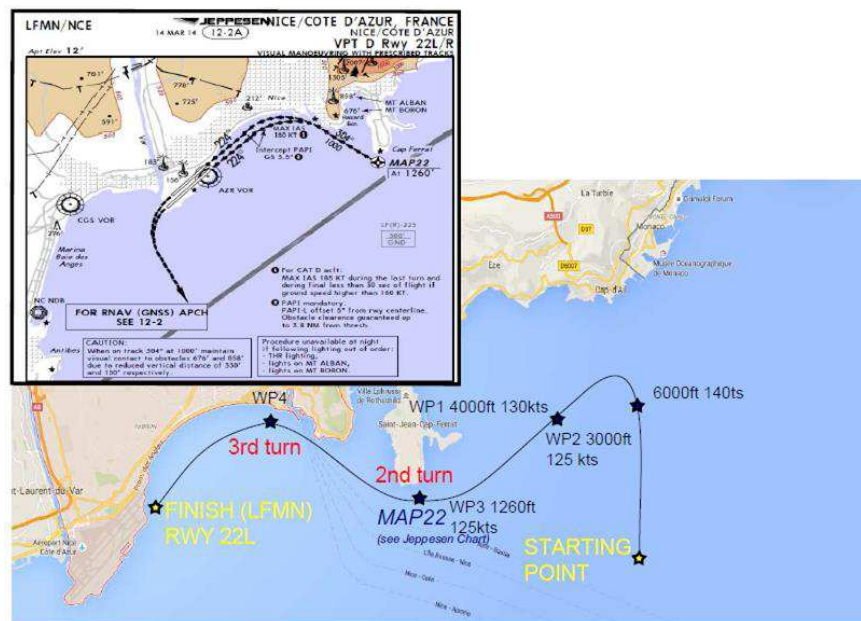
Figure 20. Flight track with waypoints towards runway 22 of Nice Côte d'Azur airport, source: Google Maps

(a) Illustration of microburst windshear phenomenon with initial aircraft position within the red rectangle, source: FAA

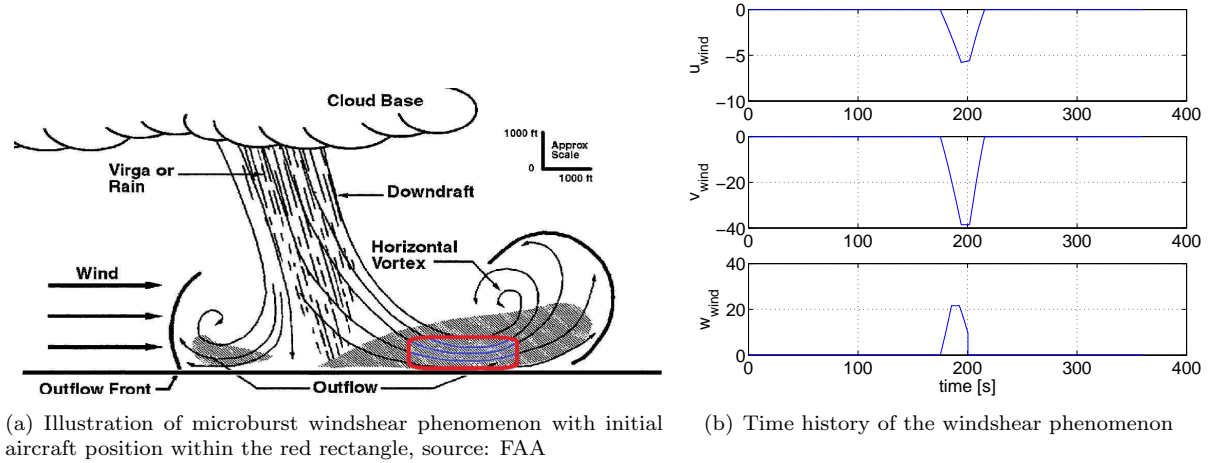(b) Time history of the windshear phenomenon

Figure 21. Setup of the windshear scenario

instant during the microburst. It is assumed that the wind components and their first order derivatives are estimated in real time during the microburst. This is a challenging assumption, but it is expected that future deployed technologies, such as airborne wind lidar sensors currently in development stage, might provide a significant contribution in this field. Purpose of this experiment scenario is to evaluate if this additional safe envelope information has an influence on the steering strategy of the pilot.

IX.   Results

Given the exploratory nature of the experiment, the fact that several technologies were evaluated and the limited number of participants, it is not possible to provide strong statistical conclusions on any particular aspect of the experiment, but the data were sufficient to observe certain trends. The evaluation results for the icing scenario are discussed first in subsection IX.A, and the windshear scenario is analyzed in subsection IX.B. In each subsection, the results from one relevant pilot are discussed first, and are then followed by a statistical analysis that covers all the pilots together.

A.   Icing scenario

A representative actual flight track of one of the participating pilots is shown in Fig. 22. Ice starts to build up in the vicinity of waypoint FL30. After WP FL10, a left hand turn is made to align the aircraft with runway 27. The simulation is ended shortly thereafter.

The time histories of some selected states and commands with current technology engaged are shown in Fig. 23, Fig. 24 shows the same states and commands with new technology. First of all, the initial speed reduction command due to the traffic ahead alert from ATC and the impact of horizontal wind gusts on all states are clearly visible. The $\max_{\text{FCL}}$ values are the maximum values as handled by the flight control laws. These values are non-adaptive for current technology in Fig. 23 and fully adaptive with the new technology as shown in Fig. 24. Moreover, Fig. 24(a) shows that a safety buffer of 2 deg. has been implemented between the true maximum angle of attack $\alpha_{\max}$ where stall occurs and the maximum angle of attack as implemented in the flight control laws $\alpha_{\max_{\text{FCL}}}$. It can be seen in Fig. 23(a) that soon after ice accretion starts, the true $\alpha_{\max}$ becomes significantly smaller than the non-adaptive $\alpha_{\max_{\text{FCL}}}$, resulting in a potentially dangerous situation. Around $t = 225s$, the true stall angle of attack is exceeded, although only very briefly, before the pilot could get in real danger. This particular experienced pilot also reported while steering that he noticed the loss of lift immediately and reacted accordingly. It was observed that less experienced pilots were not able to deal with this situation as successfully. The impact on the maximum bank angle can be seen in Fig.
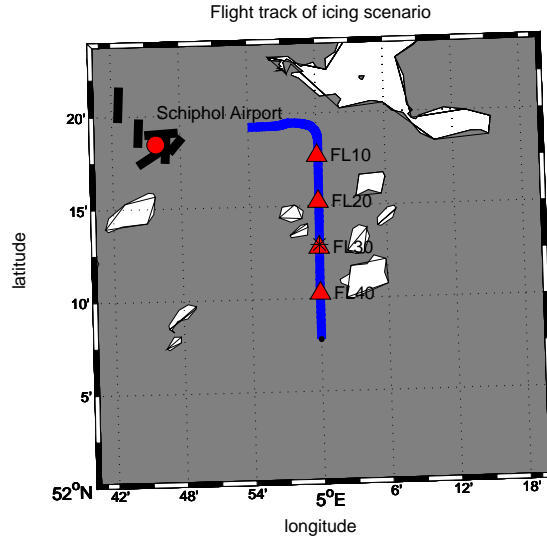
Figure 22. Flight track for icing scenario, pilot A

23(b), where the maximum bank angle is reduced by more than 10 deg because of ice accretion, without the pilot being aware of it. This leads to a potentially dangerous situation in the turn after WP FL10. The beneficial influence of the new technologies can be observed by comparing Fig. 23 and Fig. 24. The adaptive protections prevent exceeding the maximum angle of attack, and they also cut off any load factor commands that steer above the maximum permissible $\Delta n_{z_{\max}}$, which can be seen at exactly the same time as when α_{prot} is exceeded. Moreover, because of the reduced performance limits being apparent through the additional information on the PFD, the pilot chooses to increase airspeed as can be seen in Fig. 24(a) and keeps the maximum bank angle around the same value with icing as compared to the nominal configuration. The updated maximum bank angle information makes him confident enough to bank more in the turn than with current technology, while maintaining at least the same margin to the bank angle limits.

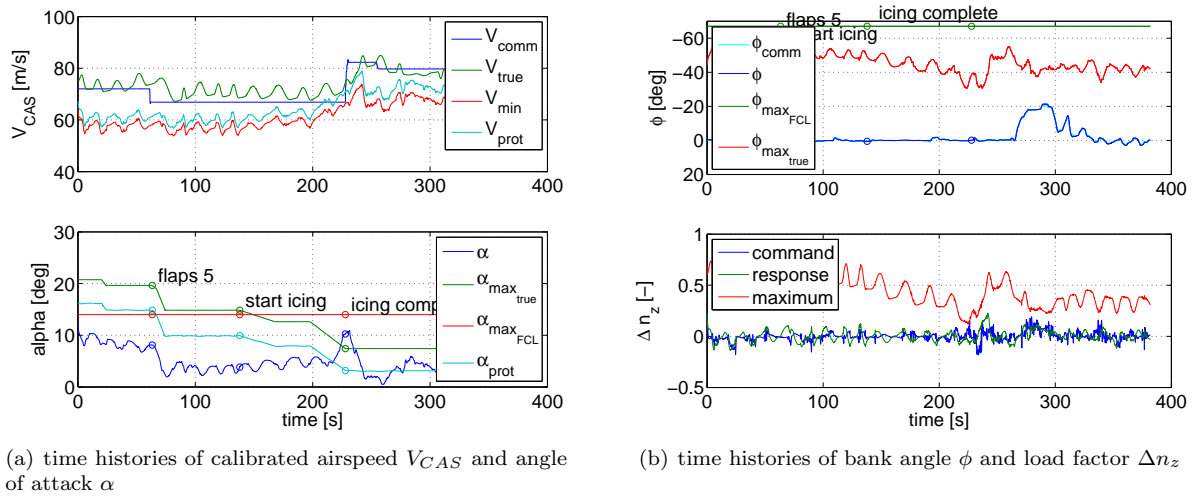(a) time histories of calibrated airspeed V_{CAS} and angle of attack α

(b) time histories of bank angle ϕ and load factor Δn_z

Figure 23. Time histories of selected states for icing scenario with current technology, pilot A

(a) time histories of calibrated airspeed V_{CAS} and angle of attack α

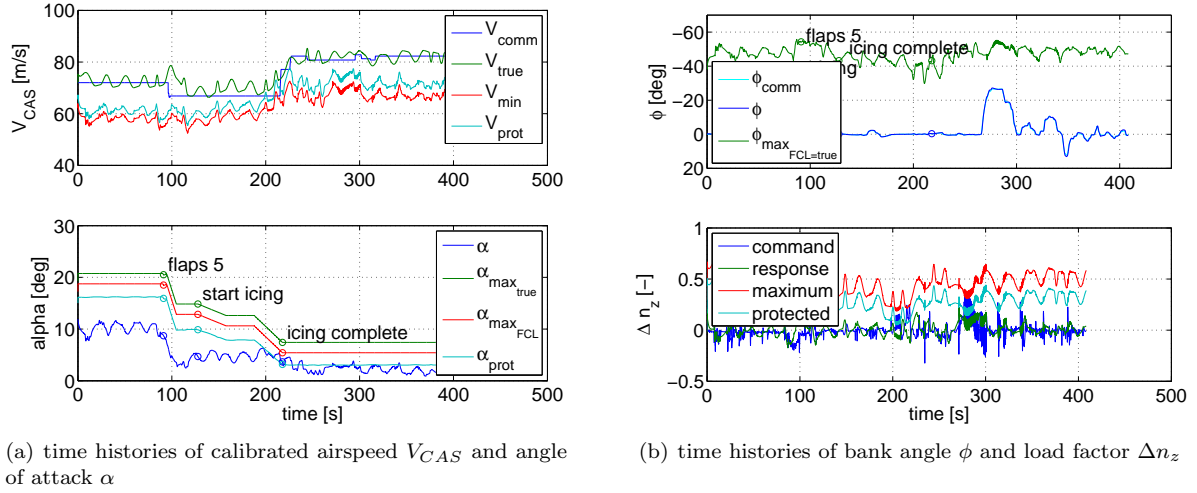(b) time histories of bank angle ϕ and load factor Δn_z

Figure 24. Time histories of selected states for icing scenario with new technology, pilot A

Figures 25, 26 and 27 show the results of the statistical analysis over all the participatants. Each figure compares the objective measures as introduced in Sec. VIII.D.1 between current technologies and new technologies. The data have been corrected for variance between subjects. On each box, the central mark is the median, the edges of the box are the 25th and 75th percentiles, the whiskers extend to the most extreme datapoints that the algorithm does not consider to be outliers, and the outliers are plotted individually. It can be clearly observed that the margins of angle of attack α, calibrated airspeed V_{CAS}, and bank angle ϕ to the envelope boundaries are significantly larger with the new technologies compared to the current technologies. These results are statistically significant. For each of these measures, the mean as well as the minimum values are considered. The mean gives an indication of the pilots steering strategy, where the minimum value is rather related to the task of disturbance rejection. Both metrics show the same beneficial trend towards the new technologies. Finally, Fig. 27 shows the mean sidestick deflection δ_{stick} as well as its deflection rate $\dot{\delta}_{\text{stick}}$. There is no significant difference between the actual deflections with current or new technology. However, the mean deflection rate is lower with new technologies, which is only a partial but quantitative indicator of decreased pilot activity and thus a lower workload, which supports the subjective pilot feedback that is discussed in Sec. C.

(a) margins angle of attack α

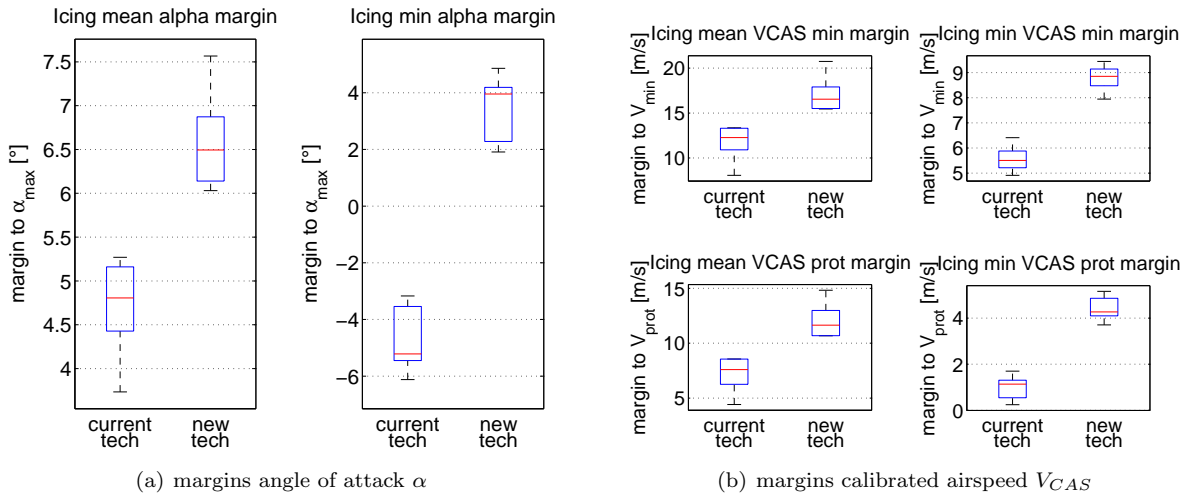(b) margins calibrated airspeed V_{CAS}

Figure 25. Statistical analysis of angle of attack and speed margins to envelope boundaries for icing scenario, all pilots
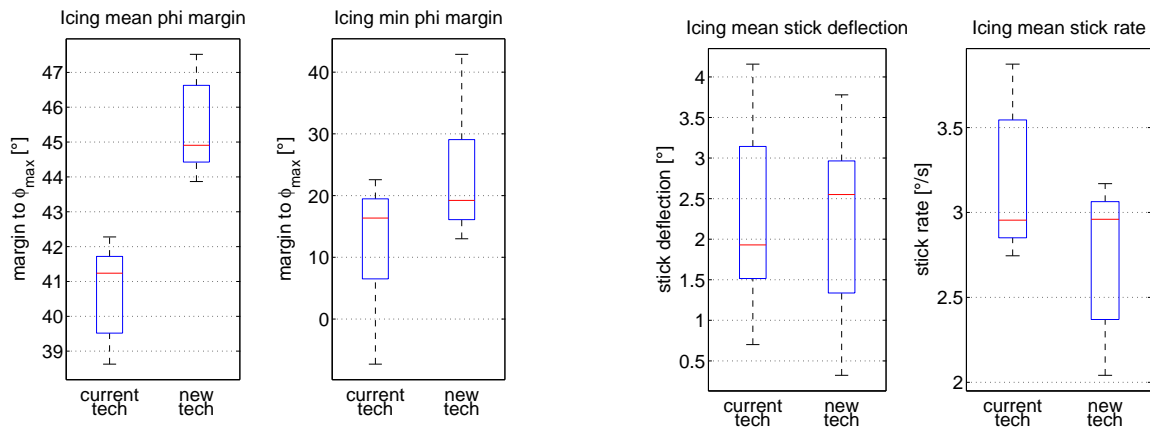

Figure 26. Statistical analysis of bank angle margin to envelope boundaries for icing scenario, all crews

Figure 27. Statictical analysis of pilot activity for icing scenario, all crews
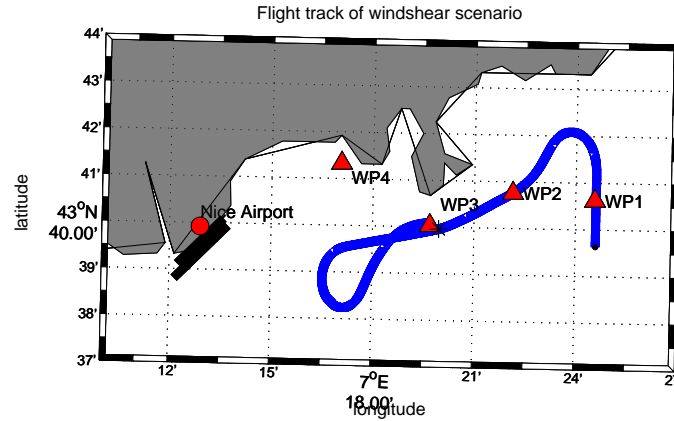
Figure 28. Flight track for windshear scenario, pilot A

B.   Windshear scenario

Fig. 28 shows a representative flight track through the previously defined waypoints along the coastline of the French Riviera, as performed by one of the experiment participants. Windshear occurs around WP3. The participating pilots were instructed to return to the position where the windshear started, once they established stabilized flight out of shear. This provides a double indication: the size of the track shows how long they needed to recover from the windshear, and the accuracy of the simulation end point is an approximate indicator of their situational awareness when the windshear started. This specific pilot demonstrated a very good performance in this respect, as can be seen in Fig. 28.

The impact of wind shear on the safe flight envelope limits can be seen in Fig. 29 and 30. The downwash followed by a tailwind lead to a significant drop in the steady vertical speed limits through the flight path angle limits $\gamma_{\min / \max}$ as shown in Fig. 29. The windshear also causes significant deviations in the airspeed compared to the commanded speed as can be seen in Fig. 30(a). Moreover, it can be seen in Fig. 30(a) that the maximum angle of attack is reached during this event, and simultaneously the maximum permissible $\Delta n_{z_{\max}}$ as shown in Fig. 30(b). Thanks to haptic feedback, the pilots feel it in the sidestick when they reach the limit of $\Delta n_{z_{\max}}$. Due to the sudden tailwind and the corresponding drop in airspeed and lift, the bank authority is reduced to zero, as shown in Fig. 30(b), which is consistent with the maximum angle of attack being met.

Despite this additional information being presented to the pilot, and the physical interpretation that is possible, no significant difference was found in the objective measures by comparing current and new technologies. During the experiments, it became clear that the pilots are trained to stick to their windshear recovery procedure, as they learn and repeat during every training session and as described in Sec. 2. It has been found that the envelope information, although being constantly updated during the whole event, did not have any noticeable impact on the observed performance measures.

A more extensive analysis of the haptics part of this study can be found in Ref. 41.

C.   Pilot Feedback

NASA TLX workload ratings in Fig. 31 show that the subjective rating of the workload by the participants decreases with the new technologies. This applies for the icing as well as for the windshear scenario, although
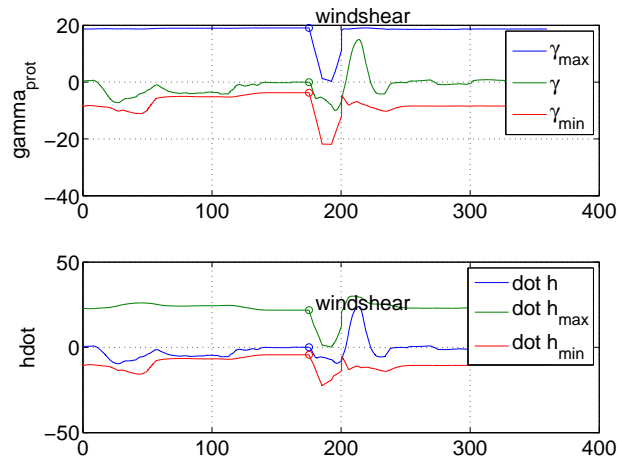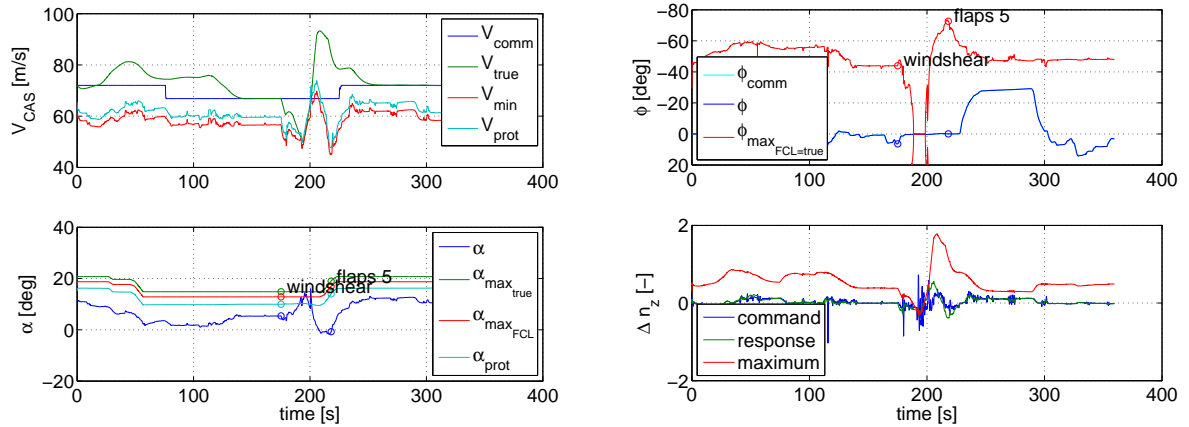
Figure 29. Time histories of flight path angle and vertical speed for the windshear scenario with new technology, pilot A

(a) time histories of calibrated airspeed V_{CAS} and angle of attack α

(b) time histories of bank angle ϕ and load factor Δn_z

Figure 30. Time histories of selected states for windshear scenario with new technology, pilot A

the trend is more apparent for windshear than for the icing scenario. All data have been corrected for variance between subjects. It should be noted that this subjective rating refers to the combination of the three new technologies mentioned before. There is no information given about the technologies individually. For the icing scenario, the subjective indication of workload in Fig. 31(a) is found to be consistent with the objective measures in Fig. 27, based on pilot activity.
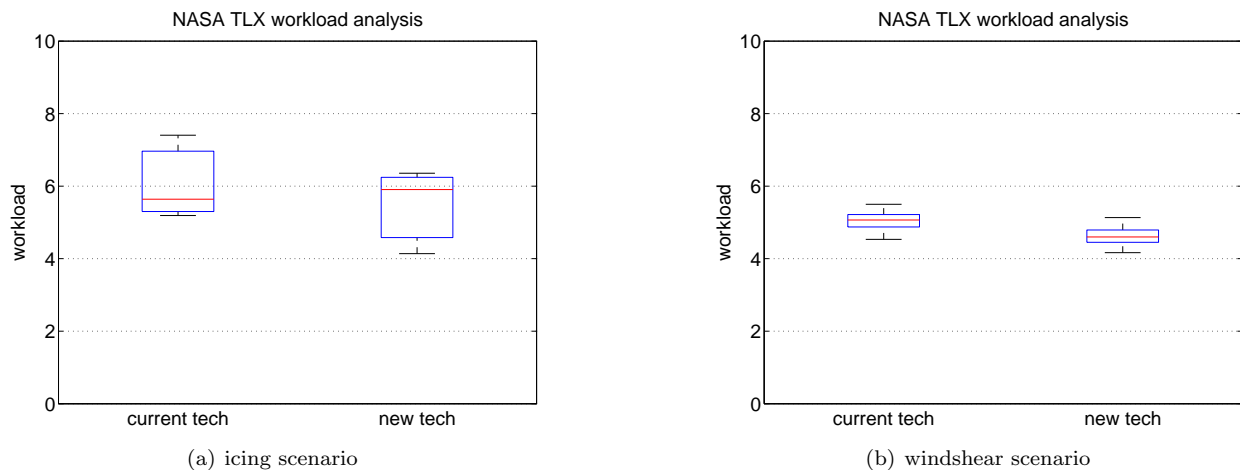

(a) icing scenario

(b) windshear scenario

Figure 31. NASA TLX workload analysis, corrected for variance between subjects

Besides the workload ratings, some questionnaires were given to the participants at the end of the study, asking about opinion ratings as well as subjective evaluations. The following observations have been made:

- *Were you, at any point during the run, confused about what the envelope protection automation was doing?* Pilots rated on average on a scale from 0 (always confused) to 10 (never confused): 8.14 (standard deviation = 1.52).

- *Please put the following (new) indications in order from the most useful for you at the top of the list to the least useful at the bottom.* Pilots rated as follows their preference: 1.Airspeed limit indication on the PFD; 2.Airspeed limit indication on the haptic stick; 3.Load factor limit indication on the haptic stick; 4.Bank angle limit indication on the PFD; 5.vertical speed speed limit indication on the PFD.

- *Please rate to what extent the new envelope limit indications changed your awareness of the scenarios you flew today compared to the current technology displays.* Pilots rated on average on a scale from 0 (decreased a lot) to 10 (increased a lot): 8.42 (standard deviation = 0.89).

- *Please indicate whether you had the feeling that you were fighting the control system.* For the icing and wind shear scenario, pilots rated on average on a scale from 0 (a lot of fighting) to 10 (not at all fighting): 7.25 (standard deviation = 2.54) and 8.71 (standard deviation = 1.16) respectively.

- *How confident are you that you were able to tell, based on the envelope information presented, what the true edges of the aircraft performance envelope were?* With the protections of the flight control laws, pilots rated on average on a scale from 0 (not at all confident) to 10 (very confident): 7.14 (standard deviation = 0.95). With the haptic protections, pilots rated on average on a scale from 0 (not at all confident) to 10 (very confident): 7.78 (standard deviation = 1.24).

In addition, it is expected that it will be easy to use the new system during peak workload situations (7.29, standard deviation 2.65), and it will be easy to learn how to use the new system (8.14, standard deviation 1.35). The new technology would help prevent a critical event from occurring (8.09, standard deviation 0.86) and help to mitigate consequences if it occurs (8.15, standard deviation 0.58). It is also expected that the new technology would reduce the likelihood of human error (7.26, standard deviation 1.16).

A few relevant verbatim comments of the experiment participants, as collected in the debriefing questionnaires, are included below:

- "Adaptive stick and stick shaker very helpful and intuitive."

- "Very valuable cues, haptics of adaptive protections makes it instinctive again to fly, and indicates limits of airplane without necessity of continuously scanning PFD. Leaves mental capacity to deal with other things or analyse situation better."

- "Windshear: good to feel aircraft become sluggish, controls not overly heavy"

- "Gives much earlier and clearer indication of state of the aircraft. Makes it easy to control aircraft accurately close to its limits. Reduces workload a lot."

- "Indicator of degraded performance is very helpful in limiting the low speeds and the high banks, especially the tactile feedback."

- "Feel more confident"

- "Adaptive airspeed limit very useful, both visual as in feedback. I also liked the bank angle limit, especially in case of go-around or after take-off."

- "Thought the heavier stick force was quite useful to identify icing, changing envelope."

The NASA TLX workload assessment scheme, as well as relevant parts of the questionnaires can be found in the appendices.

X.   Conclusion

In this research, an adaptive safe flight envelope protection algorithm has been designed and evaluated by professional commercial airline pilots in a relevant simulation environment. The algorithm makes use of a safe flight envelope estimation algorithm which calculates in real time the actual envelope bounds, taking into account malfunctions and upsets. This information about the safe envelope bounds is then used for three purposes: the bounds are displayed in an intuitive manner on the primary flight display, they are implemented as hard protections in the flight control laws, and the pilot is made aware when he approaches the envelope bounds by haptic feedback on the sidestick. This technology has been evaluated in a simulator in two relevant scenarios, namely an icing scenario and a microburst scenario. The microburst scenario did not lead to the observation of significant changes with the new technology. However, the icing scenario did. The number of pilots and repetitions were smaller than required for a full statistical analysis of the experiment, but are sufficient to observe certain trends. It has been found that with adaptive flight envelope protection, the pilot maintained significantly larger safety margins to the boundaries of the safe flight envelope and as such prevented loss of control in off-nominal conditions. Objective measures have shown a reduced workload, which is corroborated by the subjective ratings. Pilot feedback has shown that this new technology improves the situational awareness of the flight crew.

Appendix 1: NASA TLX Rating Sheet

Please fill in the following questionnaire in which you will be able to express your experiences regarding workload during each of the experiment runs and conditions. The NASA TLX questionnaire consists of two steps: in the first step you will be able to make a pairwise comparison between sources of workload. In the second step you are requested to provide the magnitude of each of the sources of workload. The description of each of the sources of workload is provided at the end of this document.[42]

Step 1 Pairwise comparison between sources of load. Make a pairwise comparison indicating which source of workload represents more accurately the previous experiment run.

☐ Mental Demand	☐ Physical Demand
☐ Mental Demand	☐ Temporal Demand
☐ Mental Demand	☐ Performance
☐ Mental Demand	☐ Effort
☐ Mental Demand	☐ Frustration Level
☐ Physical Demand	☐ Temporal Demand
☐ Physical Demand	☐ Performance
☐ Physical Demand	☐ Effort
☐ Physical Demand	☐ Frustration Level
☐ Temporal Demand	☐ Performance
☐ Temporal Demand	☐ Effort
☐ Temporal Demand	☐ Frustration Level
☐ Performance	☐ Effort
☐ Performance	☐ Frustration Level
☐ Effort	☐ Frustration Level

Step 2 Magnitude of load Indicate in what magnitude you experienced each of the sources of workload during the previous experiment run.

Mental Demand

Low   High

Physical Demand

Low   High

Temporal Demand

Low   High

Performance

Low   High

Effort

Low   High

Frustration Level

Low   High

NASA TLX rating description.

- **Mental demand:** How much mental and perceptual activity was required (e.g., thinking, deciding, remembering, looking, searching, etc.)? Was the task easy or demanding, simple or complex, exacting or forgiving?

- **Physical demand:** How much physical activity was required (e.g.. pushing, pulling, turning, controlling, activating, etc.)? Was the task easy or demanding, slow or brisk, slack or strenuous, restful or laborious?

- **Temporal demand** How much time pressure did you feel due to the rate or pace at which the tasks or task elements occurred? Was the pace slow and leisurely or rapid and frantic?

- **Effort** How successful do you think you were in accomplishing the goals of the task set by the experimenter (or yourself)? How satisfied were you with your performance in accomplishing these goals?

- **Performance** How hard did you have to work (mentally and physically) to accomplish your level of performance?

- **Frustration level** How insecure, discouraged, irritated, stressed and annoyed versus secure, gratified, content, relaxed and complacent did you feel during the task?

Appendix 2: VFR Approach Scenario Questionnaire

General questions

How would you grade the realism of the *overall* wind simulation and flight dynamics?

Unreal   Acceptable   Excellent

Comment:

Would you appreciate the haptic feedback being provided as a warning cue for flight envelope re-estimation?

Disagree   Indifferent   Agree

Comment:

In the remainder of this questionnaire a comparison between the haptics ON and OFF condition is made for each flight control law.

As compared to the haptics OFF condition, 0.9**how would you evaluate your *situational awareness* regarding unexpected variations in flight envelope?**

Worse   Indifferent   Better

Comment:

As compared to the haptics OFF condition, **how would you grade your *ability to determine* when excessive control inputs were provided[b]?**

Worse   Indifferent   Better

Comment:

As compared to the haptics OFF condition, **how would you rate the warning capability provided by the haptic feedback system during flight envelope re-estimation?**

Worse   Indifferent   Better

Comment:

---

[b]Excessive control inputs are defined as inputs which do not lead to any further change in aircraft attitude as a result of Flight Envelope Protection.

Appendix 3: Wind Shear Scenario Questionnaire

General questions

How would you grade the *overall realism* of the wind shear simulation and flight dynamics?

Unreal   Acceptable   Excellent

Comment:

Would you prefer to only feel the stick shaker without the stick force changes?

Disagree   Indifferent   Agree

Comment:

Would you appreciate the haptic feedback being provided as a control aid during the wind shear recovery procedure?

Disagree   Indifferent   Agree

Comment:

In the remainder of this questionnaire a comparison between the haptics ON and OFF condition is made for each flight control law.

As compared to the haptics OFF condition, **how would you evaluate your *situational awareness* when reaching the maximum AoA?**

Worse   Indifferent   Better

Comment:

As compared to the haptics OFF condition, **how would you grade your *ability to determine* when excessive control inputs were provided[c]?**

Worse   Indifferent   Better

Comment:

---

[c]Excessive control inputs are defined as inputs which do not lead to any further change in aircraft attitude as a result of Flight Envelope Protection.

Acknowledgments

References

[1] "Statistical Summary of Commercial Jet Airplane Accidents – Worldwide Operations 1959 - 2011," Tech. rep., Boeing Commercial Aircraft, July 2012, Available at: `http://www.boeing.com/news/techissues/pdf/statsum.pdf`. Retrieval date: October 17, 2016.

[2] "CAST Safety Enhancement Plan: Airplane State Awareness - Attitude and Energy State Awareness Technologies," Technical Report SE207, Commercial Aviation Safety Team, 2013, Available at: `http://www.skybrary.aero/index.php/Portal:CAST_SE_Plan`. Retrieval date: October 17, 2016.

[3] "CAST Safety Enhancement Plan: Airplane State Awareness - Bank Angle Protection," Technical Report SE202, Commercial Aviation Safety Team, 2013, Available at: `http://www.skybrary.aero/index.php/Portal:CAST_SE_Plan`. Retrieval date: October 17, 2016.

[4] Schuet, S., Lombaerts, T., Acosta, D., Wheeler, K., and Kaneshige, J., "Autonomous Flight Envelope Estimation for Loss-of-Control Prevention," *Journal of Guidance, Control and Dynamics*, , No. AIAA 2014-0268, 2016, DOI: 10.2514/1.g001729.

[5] Lombaerts, T., Schuet, S., Acosta, D., Kaneshige, J., Shish, K., and Martin, L., "Piloted Simulator Evaluation of Safe Flight Envelope Display Indicators for Loss of Control Avoidance," *Journal of Guidance, Control, and Dynamics*, May 2016, pp. 1–16, DOI: 10.2514/1.G001740.

[6] Brière, D., Favre, C., and Traverse, P., "A family of fault-tolerant systems: Electrical flight controls, from A320/330/340 to future military transport aircraft," *Microprocessors and Microsystems*, Vol. 19, No. 2, March 1995, pp. 75 – 82, DOI: 10.1016/0141-9331(95)98982-P.

[7] Favre, C., *Advances in Aircraft Flight Control*, chap. Fly-by-wire for commercial aircraft: the Airbus experience, Taylor & Francis, 1996, pp. 211 – 229, DOI: 10.1080/00207179408923072.

[8] Goupil, P., "AIRBUS state of the art and practices on FDI and FTC in flight control system," *Control Engineering Practice*, Vol. 19, 2011, pp. 524 – 539, DOI: 10.1016/j.conengprac.2010.12.009.

[9] Airbus, *A319/A320/A321 Flight deck and systems briefing for pilots*, September 1998, STL 945.7136/97; Available at `http://ads-b.ca/a320/A319-320-321_Flight_Deck_and_Systems_Briefing_for_Pilots.pdf`. Retrieval date: October 17, 2016.

[10] Brockhaus, R., Alles, W., and Luckner, R., *Flugregelung*, chap. A320 Regelungssystem, Springer Berlin Heidelberg, 2011, pp. 718 – 725, in German.

[11] Field, E., "The application of a C* flight control law to large civil transport aircraft," Tech. Rep. 9303, College of Aeronautics, Cranfield Institute of Technology, Cranfield, Bedford MK43 0AL, England, March 1993, Available at: `http://dspace.lib.cranfield.ac.uk/handle/1826/186`. Retrieval date: October 17, 2016.

[12] Bartley, G. F., *The Avionics Handbook*, chap. Boeing B-777: Fly-By-Wire Flight Controls, CRC Press LLC, 2001, Available at `www.davi.ws/avionics/TheAvionicsHandbook_Cap_11.pdf`. Retrieval date: October 17, 2016.

[13] McCuish, A. and Caldwell, B., "Development and flight experience of the control laws in the Experimental Aircraft Programme," *Internation Journal of Control*, Vol. 59, No. 1, 1994, pp. 183 – 198, DOI: 10.1080/00207179408923074.

[14] Lambregts, A. A., "Flight Envelope Protection for Automatic and Augmented Manual Control," *Proceedings of the EuroGNC 2013, 2nd CEAS Specialist Conference on Guidance, Navigation & Control*, 2013, pp. 1364–1383.

[15] Tang, L., Roemer, M., Ge, J., Crassidis, A., Prasad, J., and Belcastro, C., "Methodologies for Adaptive Flight Envelope Estimation and Protection," *AIAA Guidance, Navigation and Control Conference*, No. AIAA 2009-6260, August 2009, DOI: 10.2514/6.2009-6260.

[16] Krishnakumar, K., Stepanyan, V., Barlow, J., Hardy, G., Dorais, G., Poolla, C., Reardon, S., and Soloway, D., "Initial Evaluations of LoC Prediction Algorithms using the NASA Vertical Motion Simulator," *AIAA Guidance, Navigation and Control Conference*, No. AIAA 2014-0265, January 2014, DOI: 10.2514/6.2014-0265.

[17] Stepanyan, V., Krishnakumar, K., Dorais, G., Reardon, S., Barlow, J., Lampton, A., and Hardy, G., "Loss-of-Control Mitigation via Predictive Cuing," *Journal of Guidance, Control, and Dynamics*, aug 2016, DOI: 10.2514/1.G001731.

[18] Falkena, W., Borst, C., Chu, Q., and Mulder, J., "Investigation of Practical Flight Envelope Protection Systems for Small Aircraft," *Journal of Guidance, Control, and Dynamics*, Vol. 34, No. 4, jul 2011, pp. 976–988.

[19] Horn, J., Calise, A., and Prasad, J., "Flight Envelope Limit Detection and Avoidance for Rotorcraft," *Journal of the American Helicopter Society*, Vol. 47, No. 4, October 2002, pp. 253 – 262, DOI: 10.4050/JAHS.47.253.

[20] Tekles, N., Chongvisal, J., Xargay, E., Choe, R., Talleur, D. A., Hovakimyan, N., and Belcastro, C. M., "Design of a Flight Envelope Protection System for NASA's Transport Class Model," *Journal of Guidance, Control, and Dynamics*, aug 2016, pp. 1–15, DOI: 10.2514/1.G001728.

[21] Tomlin, C., Lygeros, J., and Sastry, S., "Aerodynamic Envelope Protection using Hybrid Control," *American Control Conference*, Vol. 3, IEEE, June 1998, pp. 1793 – 1796, DOI: 10.1109/ACC.1998.707322.

[22]Lombaerts, T., Looye, G., Chu, Q., and Mulder, J., "Pseudo Control Hedging and its Application for Safe Flight Envelope Protection," *AIAA Guidance, Navigation and Control Conference*, No. AIAA 2010-8280, August 2010, DOI: 10.2514/6.2010-8280.

[23]Varga, A. and Ossmann, D., "LPV model-based robust diagnosis of flight actuator faults," *Control Engineering Practice*, Vol. 31, 2013, pp. 135 147, DOI: 10.1016/j.conengprac.2013.11.004.

[24]Maskew, B., *PROGRAM VSAERO: A Computer Program for Calculating the Non-linear Aerodynamic Characteristics of Arbitrary Configurations: User's Manual*, NASA contractor report, NASA, 1982.

[25]Looye, G., "The new DLR Flight Dynamics Library," *Proceedings of the 6th Modelica Conference*, Bielefeld, Germany, 2008.

[26]FMI Steering Committee, "The Funcional Mock-up Interface," `http://www.fmi-standard.org`.

[27]Lombaerts, T. and Looye, G., "Design and flight testing of manual nonlinear flight control laws," *AIAA Guidance, Navigation and Control Conference*, No. AIAA 2011-6469, 2011, DOI: 10.2514/6.2011-6469.

[28]Lombaerts, T., *Fault Tolerant Flight Control – A Physical Model Approach*, Phd dissertation, Delft University of Technology, May 2010, Available at: `http://resolver.tudelft.nl/uuid:538b0174-fe84-43af-954d-02f256b2ec50`. Retrieval date: October 17, 2016.

[29]Hinton, D. A., "Airborne Derivation of Microburst Alerts from Ground-Based Terminal Doppler Weather Radar Information - A Flight Evaluation," Technical Memorandum 108990, NASA, August 1993.

[30]Targ, R. and Bowles, R. L., "Investigation of Airborne Lidar for Avoidance of Windshear Hazards," *Proceedings of the AIAA/NASA/AFWAL Conference on Sensors and Measurements Techniques for Aeronautical Applications*, No. AIAA-88-4658, 1988, DOI: 10.2514/6.1988-4658.

[31]Van Paassen, M. and Stroosma, O., "DUECA - Data-Driven Activation in Distributed Real-Time Computation," *AIAA Modeling and Simulation Conference and Exhibit*, No. AIAA-2000-4503, AIAA, August 2000, DOI: 10.2514/6.2000-4503.

[32]Stroosma, O., Van Paassen, M., and Mulder, M., "Using the SIMONA Research Simulator for Human-Machine Interaction Research," *AIAA Modeling and Simulation Conference and Exhibit*, No. AIAA-2003-5525, August 2003, DOI: 10.2514/6.2003-5525.

[33]Endsley, M. R., "Towards a Theory of Situation Awareness in Dynamic Systems," *Journal of Human Factors*, Vol. 37, 1995, pp. 32–64, DOI: 10.1518/001872095779049543.

[34]Hart, S. G. and Staveland, L. E., *Human Mental Workload*, chap. Development of NASA-TLX (Task Load Index): Results of Empirical and Theoretical Research, Amsterdam: North Holland Press, 1988, DOI: 10.1016/s0166-4115(08)62386-9.

[35]EASA, *CS-AWO Initial Issue*, 2003, Computer Software Manual. Available at: `https://www.easa.europa.eu/system/files/dfu/decision_ED_2003_06_RM.pdf`. Retrieval date: October 17, 2016.

[36]Khodaparast, H., Georgiou, G., Cooper, J., Riccobenne, L., Ricci, S., Vio, G., and Denner, P., "Efficient Worst Case 1-Cosine Gust Loads Prediction," *ASD Journal*, Vol. 2, 2012, pp. 33–54, DOI: 10.3293/asdj.2012.17.

[37]Vandecauter, V., *CFD simulation of atmospheric wind gusts*, Master's thesis, Delft University of Technology, 2011, Available at: `http://www.lr.tudelft.nl/fileadmin/Faculteit/LR/Organisatie/Afdelingen_en_Leerstoelen/Afdeling_AEWE/Aerodynamics/Contributor_Area/Secretary/Publications/publications/Thesis_Vincent_Vandecauter.pdf`. Retrieval date: October 17, 2016.

[38]"Windshear Training Aid," Tech. rep., FAA Federal Aviation Administration, Washington DC, USA, 1990, Available at `http://flightcrewguide.com/wp-content/uploads/2013/11/Windshear-Training-Aid-Vol-1.pdf` and `http://flightcrewguide.com/wp-content/uploads/2013/11/Windshear-Training-Aid-Vol-2.pdf`. Retrieval date: October 17, 2016.

[39]Zhenxing, G., Hongbing, G., and Hui, L., "Real-time Simulation of Large Aircraft Flying Through Microburst Windfield," *Chinese Journal of Aeronautics*, Vol. 22, No. 5, October 2009, pp. 459–466, DOI: 10.1016/S1000-9361(08)60126-0.

[40]"Adverse Weather Operations, Windshear Awareness," Flight operations briefing notes, Airbus Group, Rond Point Maurice Bellonte - 31707 BLAGNAC CEDEX France, 2007, Available at: `http://skybrary.aero/bookshelf/books/164.pdf`. Retrieval date: October 17, 2016.

[41]Ellerbroek, J., Martin, M. R., Lombaerts, T., van Paassen, M., and Mulder, M., "Design and evaluation of a Flight Envelope Protection haptic feedback system," *IFAC-PapersOnLine*, Vol. 49, No. 19, 2016, pp. 171–176, DOI: 10.1016/j.ifacol.2016.10.481.

[42]Hart, Sandra, G., "NASA-task load index (NASA-TLX); 20 years later," *Human Factors and Ergonomics Society Annual Meting*, 2006, pp. 904–908.